SPT-GMOS: A GEMINI/GMOS-SOUTH SPECTROSCOPIC SURVEY OF GALAXY CLUSTERS IN THE SPT-SZ SURVEY

M. B. BAYLISS[1,2,3], J. RUEL[1], C. W. STUBBS[1,2], S. W. ALLEN[4,5,6], D. E. APPLEGATE[7], M. L. N. ASHBY[2], M. BAUTZ[8], B. A. BENSON[9,10,11], L. E. BLEEM[10,12,13], S. BOCQUET[10,13,14,15], M. BRODWIN[16], R. CAPASSO[14,15] J. E. CARLSTROM[9,10,12,13,17], C. L. CHANG[9,10,13], I. CHIU[14,15], H-M. CHO[18], A. CLOCCHIATTI[19], T. M. CRAWFORD[9,10] A. T. CRITES[20], T. DE HAAN[21, 22], S. DESAI[14,15], J. P. DIETRICH[14,15], M. A. DOBBS[22,23], A. N. DOUCOULIAGOS[24], R. J. FOLEY[25,26,27], W. R. FORMAN[2], G. P. GARMIRE[28], E. M. GEORGE[21,29], M. D. GLADDERS[9,10], A. H. GONZALEZ[30], N. GUPTA[14,15], N. W. HALVERSON[31], J. HLAVACEK-LARRONDO[32,33,5], H. HOEKSTRA[34], G. P. HOLDER[22], W. L. HOLZAPFEL[21], Z. HOU[10,12], J. D. HRUBES[35], N. HUANG[21], C. JONES[2], R. KEISLER[10,4,5,12], L. KNOX[36], A. T. LEE[21,37], E. M. LEITCH[9,10], A. VON DER LINDEN[38,39,4,5], D. LUONG-VAN[35], A. MANTZ[10,4,5], D. P. MARRONE[40], M. MCDONALD[8], J. J. MCMAHON[41], S. S. MEYER[9,10,12,17], L. M. MOCANU[9,10], J. J. MOHR[29,14,15], S. S. MURRAY[2], S. PADIN[9,10,20], C. PRYKE[42], D. RAPETTI[14, 15], C. L. REICHARDT[24], A. REST[43], J. E. RUHL[44], B. R. SALIWANCHIK[44], A. SARO[14, 15], J. T. SAYRE[31], K. K. SCHAFFER[10,17,45], T. SCHRABBACK[7], E. SHIROKOFF[9,10], J. SONG[41,46], H. G. SPIELER[37], B. STALDER[2], S. A. STANFORD[36,47], Z. STANISZEWSKI[44], A. A. STARK[2], K. T. STORY[4,5], K. VANDERLINDE[48,49], J. D. VIEIRA[26,27], A. VIKHLININ[2], R. WILLIAMSON[9,10,20], AND A. ZENTENO[50]

Draft version September 20, 2016

ABSTRACT

We present the results of SPT-GMOS, a spectroscopic survey with the Gemini Multi-Object Spectrograph (GMOS) on Gemini South. The targets of SPT-GMOS are galaxy clusters identified in the SPT-SZ survey, a millimeter-wave survey of 2500 deg^2 of the southern sky using the South Pole Telescope (SPT). Multi-object spectroscopic observations of 62 SPT-selected galaxy clusters were performed between January 2011 and December 2015, yielding spectra with radial velocity measurements for 2595 sources. We identify 2243 of these sources as galaxies, and 352 as stars. Of the galaxies, we identify 1579 as members of SPT-SZ galaxy clusters. The primary goal of these observations was to obtain spectra of cluster member galaxies to estimate cluster redshifts and velocity dispersions. We describe the full spectroscopic dataset and resulting data products, including galaxy redshifts, cluster redshifts and velocity dispersions, and measurements of several well-known spectral indices for each galaxy: the equivalent width, W, of [O II] $\lambda\lambda3727,3729$ and H-δ, and the 4000Å break strength, D4000. We use the spectral indices to classify galaxies by spectral type (i.e., passive, post-starburst, star-forming), and we match the spectra against photometric catalogs to characterize spectroscopically-observed cluster members as a function of brightness (relative to m*). Finally, we report several new measurements of redshifts for ten bright, strongly-lensed background galaxies in the cores of eight galaxy clusters. Combining the SPT-GMOS dataset with previous spectroscopic follow-up of SPT-SZ galaxy clusters results in spectroscopic measurements for > 100 clusters, or $\sim 20\%$ of the full SPT-SZ sample.

Subject headings: Catalogs — Galaxies: clusters: general — galaxies: distances and redshifts — techniques: spectroscopic

mbbayliss@cfa.harvard.edu

[1] Department of Physics, Harvard University, 17 Oxford Street, Cambridge, MA 02138
[2] Harvard-Smithsonian Center for Astrophysics, 60 Garden Street, Cambridge, MA 02138
[3] Department of Physics and Astronomy, Colby College, 5100 Mayflower Hill Dr, Waterville, ME 04901
[21] Department of Physics, University of California, Berkeley, CA, USA 94720
[22] Department of Physics, McGill University, Montreal, Quebec H3A 2T8, Canada
[9] Department of Astronomy and Astrophysics, University of Chicago, Chicago, IL, USA 60637
[10] Kavli Institute for Cosmological Physics, University of Chicago, Chicago, IL, USA 60637
[11] Fermi National Accelerator Laboratory, Batavia, IL 60510-0500, USA
[12] Department of Physics, University of Chicago, Chicago, IL, USA 60637
[13] Argonne National Laboratory, Argonne, IL, USA 60439
[4] Kavli Institute for Particle Astrophysics and Cosmology, Stanford University, 452 Lomita Mall, Stanford, CA 94305
[5] Department of Physics, Stanford University, 382 Via Pueblo Mall, Stanford, CA 94305

[6] SLAC National Accelerator Laboratory, 2575 Sand Hill Road, Menlo Park, CA 94025
[7] Argelander-Institut für Astronomie, Auf dem Hügel 71, D-53121 Bonn, Germany
[8] Kavli Institute for Astrophysics and Space Research, Massachusetts Institute of Technology, 77 Massachusetts Avenue, Cambridge, MA 02139
[14] Faculty of Physics, Ludwig-Maximilians-Universität, Scheinerstr. 1, 81679 Munich, Germany
[15] Excellence Cluster Universe, Boltzmannstr. 2, 85748 Garching, Germany
[16] Department of Physics and Astronomy, University of Missouri, 5110 Rockhill Road, Kansas City, MO 64110
[17] Enrico Fermi Institute, University of Chicago, Chicago, IL, USA 60637
[18] NIST Quantum Devices Group, Boulder, CO, USA 80305
[19] Departamento de Astronomia y Astrosifica, Pontificia Universidad Catolica,Chile
[20] California Institute of Technology, Pasadena, CA, USA 91125
[23] Canadian Institute for Advanced Research, CIFAR Program in Cosmology and Gravity, Toronto, ON, M5G 1Z8, Canada

1. INTRODUCTION

Precise spectroscopic measurements of the recession velocities of distant galaxies are among the most important cosmological observables available for studying large scale structure in the universe (Geller & Huchra 1989; Colless et al. 2001, 2003; Eisenstein et al. 2005; Geller et al. 2005; Drinkwater et al. 2010; Eisenstein et al. 2011; Geller et al. 2014). On cosmological scales, galaxy line-of-sight recession velocities increase monotonically, on average, with their distance; this bulk recession velocity is known as the Hubble Flow (Hubble & Humason 1931). The line-of-sight velocities of individual galaxies are perturbed off of the Hubble Flow via two distinct kinds of gravitational interactions: gravitational redshifts, as described by general relativity (e.g., Chant 1930), and peculiar velocities induced by local gradients in the matter density (e.g., Jackson 1972; Kaiser 1987). The former effect is typically very small (~ 11km s^{-1} Wojtak et al.

[24] School of Physics, University of Melbourne, Parkville, VIC 3010, Australia
[25] Department of Astronomy and Astrophysics, University of California, Santa Cruz, CA 95064, USA
[26] Astronomy Department, University of Illinois at Urbana-Champaign, 1002 W. Green Street, Urbana, IL 61801, USA
[27] Department of Physics, University of Illinois Urbana-Champaign, 1110 W. Green Street, Urbana, IL 61801, USA
[28] Huntingdon Institute for X-ray Astronomy, LLC
[29] Max Planck Institute for Extraterrestrial Physics, Giessenbachstr. 1, 85748 Garching, Germany
[30] Department of Astronomy, University of Florida, Gainesville, FL 32611
[31] Department of Astrophysical and Planetary Sciences and Department of Physics, University of Colorado, Boulder, CO, USA 80309
[32] Department of Physics, Université de Montréal, Montreal, Quebec H3T 1J4, Canada
[33] Kavli Institute for Particle Astrophysics and Cosmology, Stanford University, 452 Lomita Mall, Stanford, CA 94305-4085, USA
[34] Leiden Observatory, Leiden University, Niels Bohrweg 2, 2333 CA, Leiden, the Netherlands
[35] University of Chicago, Chicago, IL, USA 60637
[36] Department of Physics, University of California, Davis, CA, USA 95616
[37] Physics Division, Lawrence Berkeley National Laboratory, Berkeley, CA, USA 94720
[38] Department of Physics and Astronomy, Stony Brook University, Stony Brook, NY 11794, USA
[39] Dark Cosmology Centre, Niels Bohr Institute, University of Copenhagen Juliane Maries Vej 30, 2100 Copenhagen, Denmark
[40] Steward Observatory, University of Arizona, 933 North Cherry Avenue, Tucson, AZ 85721
[41] Department of Physics, University of Michigan, Ann Arbor, MI, USA 48109
[42] Department of Physics, University of Minnesota, Minneapolis, MN, USA 55455
[43] Space Telescope Science Institute, 3700 San Martin Dr., Baltimore, MD 21218
[44] Physics Department, Center for Education and Research in Cosmology and Astrophysics, Case Western Reserve University,Cleveland, OH, USA 44106
[45] Liberal Arts Department, School of the Art Institute of Chicago, Chicago, IL, USA 60603
[46] Korea Astronomy and Space Science Institute, Daejeon 305-348, Republic of Korea
[47] Institute of Geophysics and Planetary Physics, Lawrence Livermore National Laboratory, Livermore, CA 94551
[48] Dunlap Institute for Astronomy & Astrophysics, University of Toronto, 50 St George St, Toronto, ON, M5S 3H4, Canada
[49] Department of Astronomy & Astrophysics, University of Toronto, 50 St George St, Toronto, ON, M5S 3H4, Canada
[50] Cerro Tololo Inter-American Observatory, Casilla 603, La Serena, Chile

2011; Sadeh et al. 2015) and rarely observed, but the latter is a standard tool for constraining the statistical properties of density fluctuations on large scales (redshift space distortions, e.g., Percival & White 2009) and for measuring the depths of the gravitational potential wells of individual large fluctuations, namely clusters of galaxies (Dressler et al. 1999; Rines et al. 2003; White et al. 2010; Rines et al. 2013; Geller et al. 2013; Saro et al. 2013; Sifón et al. 2013; Ruel et al. 2014; Bocquet et al. 2015; Kirk et al. 2015; Sifón et al. 2016).

The first large samples of galaxy clusters were identified as over-densities of galaxies (Abell 1958), and have more recently been identified out to high redshift using optical and near-infrared observations (e.g.; Gladders & Yee 2000; Koester et al. 2007; Eisenhardt et al. 2008; Wen et al. 2012; Rykoff et al. 2014). Galaxy clusters are also identifiable from the observational signatures associated with the hot, diffuse intracluster gas that accounts for the vast majority of their baryonic content, and there is a long history in the literature of galaxy cluster samples based on the characteristic extended X-ray emission that results from that hot intracluster gas (e.g.; Edge et al. 1990; Ebeling et al. 1998; Rosati et al. 1998; Böhringer et al. 2000, 2001; Burenin et al. 2007; Pacaud et al. 2016).

In recent years astronomers have been able to produce dedicated surveys at millimeter wavelengths that identify massive galaxy clusters via the Sunyaev Zel'dovich (SZ) effect (Sunyaev & Zel'dovich 1972; Sunyaev & Zel'dovich 1980). The *Planck* satellite (Planck Collaboration et al. 2014), the Atacama Cosmology Telescope (ACT; Marriage et al. 2011; Hasselfield et al. 2013), and the South Pole Telescope (Staniszewski et al. 2009; Vanderlinde et al. 2010; Williamson et al. 2011; Reichardt et al. 2013; Bleem et al. 2015) have all published SZ-based galaxy cluster catalogs. Galaxy cluster surveys that select clusters based on the SZ effect and have sufficient angular resolution to resolve galaxy clusters at all redshifts (e.g., SPT and ACT with $\sim 1'$ beams) benefit from an approximately flat selection in mass beyond $z \gtrsim 0.25$ (Carlstrom et al. 2002), which results in clean, mass-selected samples extending well beyond a redshift of $z = 1$. These SZ-selected galaxy cluster samples present us with new opportunities to characterize the properties of galaxy clusters in well-defined bins of mass and redshift. Such samples can be powerful tools for testing cosmological models via the growth of structure (e.g., Planck Collaboration et al. 2014; de Haan et al. 2016), and for understanding the astrophysical processes that govern how galaxies evolve in the most overdense environments (e.g., Zenteno et al. 2011; Bayliss et al. 2014a; Chiu et al. 2016; Hennig et al. 2016; McDonald et al. 2016; Sifón et al. 2016; Zenteno et al. 2016)

In this work we present spectroscopic observations from SPT-GMOS — a large NOAO survey program (11A-0034, PI: C. Stubbs) using the Gemini Multi-Object Spectrograph (GMOS; Hook et al. 2004) on Gemini-South. The objective of this program was to measure cosmological redshifts of cluster member galaxies and other galaxies along the line of sight toward galaxy clusters that were identified in the SPT-SZ survey (Bleem et al. 2015). In this work we describe observations of 62 galaxy clusters carried out between September 2011 and May 2015. This program can be combined with numerous smaller programs to obtain spectroscopic

FIG. 1.— The full 2500 deg^2 SPT-SZ sample of 516 confirmed galaxy clusters (black dots) with the 62 SPT-GMOS clusters marked with red stars. Redshifts and masses for the full SPT-SZ sample are those described in Bleem et al. (2015), where three clusters only have approximate redshift lower limits based on *Spitzer* infrared imaging.

observations of SPT clusters (Brodwin et al. 2010; Foley et al. 2011; Stalder et al. 2013; Bayliss et al. 2014a; Ruel et al. 2014) to produce a sample of ~ 100 SPT clusters that have been followed up with multi-object spectroscopy (MOS).

Throughout the paper, we assume a standard Lambda Cold Dark Matter (ΛCDM) cosmology with $\Omega_M = 0.3$, $\Omega_\Lambda = 0.7$, $\sigma_8 = 0.8$, $H_0 = 70$ km s^{-1} Mpc^{-1}, and $h = H_0/100 = 0.7$. All quoted magnitudes are in the AB system.

2. THE SPT-GMOS SURVEY AND OBSERVATIONS

2.1. *Motivation and Design*

SPT-GMOS was motivated by the challenge of calibrating mass-observable relations for galaxy clusters, and the reality that current cosmological constraints from galaxy cluster counts are systematically limited by uncertainty in estimating cluster masses (Majumdar & Mohr 2003, 2004; Rozo et al. 2010; Williamson et al. 2011; Benson et al. 2013; Planck Collaboration et al. 2014; von der Linden et al. 2014; Bocquet et al. 2015; de Haan et al. 2016). The primary goal of the SPT-GMOS survey is to measure line-of-sight velocity dispersions for a large fraction of the SPT-SZ galaxy cluster sample. These dispersions can be combined with other mass-proxies (X-ray, weak lensing) to more accurately calibrate the SZ-mass scaling relation so that precise dark energy constraints can be obtained using the SPT cluster sample. To this end, the SPT-GMOS program represents a survey-level investment of resources to expand the sample of velocity dispersion measurements that we have for SPT-SZ galaxy clusters. The survey results presented here greatly expand upon previously published spectroscopic measurements of SPT clusters that were obtained through numerous observing programs (Ruel et al. 2014), including the results of the first semester of SPT-GMOS spectroscopy.

The data presented in this paper follow the same observational design described by Ruel et al. (2014). Specifically, we pursue a relatively "low-N" strategy to measure velocity dispersions for a large number of clusters using typically $N \lesssim 40$ cluster members. This strategy allows us to efficiently observe a large number of galaxy clusters; we design two multi-object spectroscopic masks for each cluster, generally placing slits on approximately $60 - 70$ galaxies within a $\sim 3'$ radius of the center of each targeted galaxy cluster. The efficiency advantage of this approach is twofold. Firstly, by pursuing $\lesssim 40$ cluster member galaxies we avoid reliance on measuring redshifts for extremely faint cluster members, which means that we require significantly less integration time for each spectroscopic mask. In practice this means that all of the masks observed in the SPT-GMOS program are exposed for less than 1.9hrs, and the vast majority for less than 1.5hrs. Secondly, we require only two spectroscopic masks per cluster, which results in a total integration time investment that is always less than < 3.8hrs per cluster, and less than < 2.5hrs per cluster for the vast majority ($\sim 80\%$) of observed clusters (see Table 1). The final Gemini-S observing allocation for SPT-GMOS concluded at the end of the 2015B semester. Over the course of the entire survey we observed 121 individual spectroscopic masks targeting 62 SPT-SZ galaxy clusters.

All final data products from SPT-GMOS are publicly released via the Harvard Dataverse Network[51], which has hosted all partial SPT-GMOS data releases to date.

2.2. *The South Pole Telescope Galaxy Cluster Sample*

The galaxy clusters observed in the SPT-GMOS are all drawn from the SPT-SZ survey, completed in November 2011 (Carlstrom et al. 2011). The full SPT-SZ survey covered approximately 2500 deg^2 of the southern sky at 95, 150, and 220 GHz with an angular resolution of $\sim 1'$. Noise levels in the SPT maps are ~ 40, 18, and 70 μK-arcmin in the 95, 150, and 220 GHz bands, respectively. Galaxy cluster candidates were identified in the SPT-SZ survey via the signal imprinted by the inverse Compton scattering of cosmic microwave background (CMB) photons off of hot intra-cluster gas, i.e., via the thermal SZ effect.

The full SPT-SZ galaxy cluster sample contains 409 (677) cluster candidates with SZ detection significance, $\xi_{\rm SPT} \geq 5(4.5)$, with the $\xi_{\rm SPT} \geq 5$ candidates having a measured purity of 95% (Song et al. 2012; Bleem et al. 2015). The SPT cluster selection extends to high redshift (e.g., $z \sim 1.5$ Bayliss et al. 2014a) and is approximately flat in mass beyond $z \sim 0.25$, with a mass threshold of $M_{500c} \gtrsim 5 \times 10^{14}\ M_\odot\ h_{70}^{-1}$ at $z = 0.25$, and $M_{500c} \gtrsim 3 \times 10^{14}\ M_\odot\ h_{70}^{-1}$ at $z > 1.0$ (Figure 1; Benson et al. 2013; Bocquet et al. 2015; de Haan et al. 2016), where M_{500c} refers to the mass contained within the radius for which the mean enclosed density is 500 times the critical density of the universe. For more information regarding the survey strategy and data analysis we direct the reader to the publications describing the SPT-SZ survey and resulting cluster catalogs in detail (Staniszewski

---

[51] https://dataverse.harvard.edu/dataverse/SPT_Clusters

et al. 2009; Vanderlinde et al. 2010; Schaffer et al. 2011; Reichardt et al. 2013; Bleem et al. 2015).

2.3. *Gemini/GMOS-South Spectroscopy*
2.3.1. *Selecting Cluster Targets*

Individual target selection for GMOS spectroscopy was determined by three main factors:

- First consideration was given to clusters that are being targeted as part of a broad program to support multi-wavelength mass calibration of SPT-SZ galaxy clusters. Where possible we obtained SPT-GMOS spectroscopy for systems that already had weak lensing and/or X-ray data.

- The pool of available SPT-SZ clusters changed over the four year lifetime of the SPT-GMOS survey because the full SPT-SZ galaxy cluster catalog was not finalized until approximately two years after SPT-GMOS spectroscopic observations began.

- SPT-GMOS targets were restricted to a redshift range of $0.3 < z < 0.8$ for the first four years of survey observations due to the limitations inherent to the *e2v* detectors that were used in GMOS-South prior to the 2014B semester.

The ultimate goal was to obtain comprehensive multi-wavelength follow-up for as many SPT-SZ clusters as possible, which will optimize the potential for scaling relation analyses using SZ, X-ray, lensing, and dynamical observables. Other mature SPT-SZ cluster follow-up programs include a large *Chandra-XVP* (PI: B. Benson; see McDonald et al. 2013, 2014), and weak lensing programs (High et al. 2012). These programs are converging toward a sample of $\sim$100 SPT-SZ clusters that have spectroscopic/velocity dispersions, weak lensing measurements, and X-ray observations.

In practice, the SPT-GMOS cluster targets were chosen preferentially from the higher significance — and higher mass/purity — SPT galaxy cluster candidates (generally $\xi_{SPT} > 5$), though some lower-significance clusters were observed because target selection was a rolling process. Specifically, the spectroscopic observations began in 2011A, prior to the completion of the full 2500 deg^2 SPT-SZ survey, resulting in spectroscopic targets for the first two years of the program being drawn from only a fraction of the ultimate 2500 deg^2 survey area — primarily from the first 720 deg^2 (Reichardt et al. 2013).

Target selection for the SPT-GMOS survey program was further constrained to focus on low and moderate redshift clusters from the SPT sample, specifically those within the redshift range $0.3 < z < 0.8$, as estimated from red-sequence based photometric redshifts (Song et al. 2012; Bleem et al. 2015). We chose this range because it was a good match to the capabilities of the original GMOS-South instrument. Prior to August 2014 GMOS-South used thinned *e2v* detectors designed to optimize throughput in the blue ($\lambda \lesssim 6000$Å) while sacrificing quantum efficiency in the red; these detectors also exhibit severe fringing at redder ($\lambda \gtrsim 7300$Å) wavelengths. The poor performance in the red made GMOS-South a suboptimal choice for pursuing galaxy redshifts beyond $z = 0.8$, where most of the strong spectral features that are common in cluster member galaxy spectra — e.g., Ca II H&K, H-δ, G-band, and Hγ — are redshifted into the fringe-affected wavelength range.

The final SPT-GMOS sample is plotted relative to the full SPT-SZ 2500 deg^2 cluster sample in Figure 1, and the complete SPT-GMOS list of clusters observed through early May 2015 is given in Table 1. Observations are complete for 121 custom spectroscopic slit-masks targeting 62 individual galaxy cluster fields. Additional observations remained active in the Gemini-South queue throughout 2015. Reduction of observations taken through the end of the 2015B are in progress and will be made publicly available alongside the data presented here. As of 2014B the GMOS detector was upgraded to new red-sensitive chips, and we relaxed the $z < 0.8$ redshift constraint for selected cluster targets beginning in that semester.

TABLE 1
Gemini/GMOS-South Observations of SPT-SZ Galaxy Clusters

Cluster	RA	Dec	ξ_{SPT}	Program ID	Mask	Grating	Filter	λ_c (Å)	t_{exp} (s)
SPT-CL J0013-4906	00:13:19.0	-49:06:54	11.22	GS-2012A-Q-37	01	B600_G5323	—	5400, 5500	2200
				GS-2012A-Q-37	02	B600_G5323	—	5400, 5500	2200
SPT-CL J0033-6326	00:33:54.4	-63:26:46	7.50	GS-2012B-Q-29	05	B600_G5323	—	6000, 6100	2600
				GS-2012B-Q-29	06	B600_G5323	—	5900, 6000	2600
SPT-CL J0040-4407	00:40:49.2	-44:07:58	19.34	GS-2011A-C-03	09	B600_G5323	—	5200, 5250	2100
				GS-2011A-C-03	10	B600_G5323	—	5200, 5250	2100
SPT-CL J0102-4603	01:02:40.6	-46:03:53	7.33	GS-2012B-Q-29	13	R400_G5325	GG455_G0329	7000, 7100	5760
				GS-2012B-Q-29	14	R400_G5325	GG455_G0329	7000, 7100	5760
SPT-CL J0106-5943	01:06:27.7	-59:43:16	9.57	GS-2012B-Q-59	13	B600_G5323	—	5800, 5900	2400
				GS-2012B-Q-59	14	B600_G5323	—	5800, 5900	2400
SPT-CL J0118-5156	01:18:23.8	-51:56:36	5.97	GS-2011B-C-06	52	R400_G5325	GG455_G0329	6600, 6650	4560
				GS-2011B-C-06	53	R400_G5325	GG455_G0329	6600, 6650	4560
SPT-CL J0123-4821	01:23:10.1	-48:21:31	6.92	GS-2012B-Q-29	23	R400_G5325	GG455_G0329	7000, 7100	5760
SPT-CL J0142-5032	01:42:10.8	-50:32:37	10.12	GS-2012B-Q-29	21	R400_G5325	GG455_G0329	7000, 7100	4800
				GS-2012B-Q-29	22	R400_G5325	GG455_G0329	7000, 7100	4800
SPT-CL J0200-4852	02:00:34.5	-48:52:32	7.38	GS-2012B-Q-29	07	B600_G5323	—	5800, 5900	2500
				GS-2012B-Q-29	08	B600_G5323	—	5800, 5900	2500

TABLE 1 — *Continued*

Cluster	RA	Dec	ξ_{SPT}	Program ID	Mask	Grating	Filter	λ_c (Å)	t_{exp} (s)
SPT-CL J0205-6432	02:05:07.1	-64:32:44	5.83	GS-2011B-C-06	56	R400_G5325	GG455_G0329	6600, 6650	4800
				GS-2011B-C-06	57	R400_G5325	GG455_G0329	6600, 6650	4800
SPT-CL J0212-4657	02:12:25.5	-46:57:00	10.05	GS-2012B-Q-29	19	R400_G5325	GG455_G0329	6600, 6700	3600
				GS-2012B-Q-29	20	R400_G5325	GG455_G0329	6600, 6700	3600
SPT-CL J0233-5819	02:33:01.3	-58:19:38	6.55	GS-2011B-C-06	54	R400_G5325	GG455_G0329	6600, 6650	4800
SPT-CL J0243-4833	02:43:39.3	-48:33:36	13.90	GS-2012B-Q-29	03	R400_G5325	—	6000, 6100	2600
				GS-2012B-Q-29	04	R400_G5325	—	6000, 6100	3900
SPT-CL J0243-5930	02:43:26.8	-59:30:44	7.67	GS-2012B-Q-29	09	R400_G5325	GG455_G0329	6600, 6700	4200
				GS-2012B-Q-29	10	R400_G5325	GG455_G0329	6600, 6700	4200
SPT-CL J0245-5302	02:45:30.7	-53:02:09	...[a]	GS-2011A-C-03	01	B600_G5323	—	5200, 5250	1500
				GS-2011A-C-03	02	B600_G5323	—	5200, 5250	1500
SPT-CL J0252-4824	02:52:45.1	-48:24:44	7.03	GS-2013B-Q-72	07	B600_G5323	—	5800, 5900	2200
				GS-2013B-Q-72	08	B600_G5323	—	5800, 5900	2200
SPT-CL J0304-4401	03:04:16.8	-44:01:53	15.69	GS-2012B-Q-59	05	R400_G5325	GG455_G0329	6100, 6200	3000
				GS-2012B-Q-59	06	R400_G5325	GG455_G0329	6100, 6200	3000
SPT-CL J0307-6225	03:07:20.1	-62:25:57	8.46	GS-2012B-Q-29	01	R400_G5325	GG455_G0329	6200, 6300	3600
				GS-2012B-Q-29	02	R400_G5325	GG455_G0329	6200, 6300	3600
SPT-CL J0310-4647	03:10:31.0	-46:47:00	7.12	GS-2013B-Q-72	11	R400_G5325	GG455_G0329	6700, 6800	3800
				GS-2013B-Q-72	12	R400_G5325	GG455_G0329	6700, 6800	3800
SPT-CL J0324-6236	03:24:12.7	-62:36:07	8.75	GS-2013B-Q-25	09	R400_G5325	GG455_G0329	7000, 7100	5760
				GS-2013B-Q-25	10	R400_G5325	GG455_G0329	7000, 7100	5760
SPT-CL J0334-4659	03:34:11.1	-46:59:35	9.20	GS-2013B-Q-72	13	B600_G5323	—	5800, 5900	2400
				GS-2013B-Q-72	14	B600_G5323	—	5800, 5900	2400
SPT-CL J0348-4515	03:48:17.7	-45:15:03	10.12	GS-2012B-Q-59	01	B600_G5323	—	5400, 5500	1600
				GS-2012B-Q-59	02	B600_G5323	—	5400, 5500	1600
SPT-CL J0352-5647	03:52:56.8	-56:47:58	7.13	GS-2013B-Q-25	11	R400_G5325	GG455_G0329	6800, 6900	4800
				GS-2013B-Q-25	12	R400_G5325	GG455_G0329	6800, 6900	4800
SPT-CL J0356-5337	03:56:20.5	-53:37:59	6.02	GS-2014B-Q-31	03	R400_G5325	GG455_G0329	7800, 8000	4800
				GS-2014B-Q-31	04	R400_G5325	GG455_G0329	7800, 8000	6600
SPT-CL J0403-5719	04:03:52.3	-57:19:25	5.86	GS-2012B-Q-59	07	B600_G5323	—	5600, 5700	2000
				GS-2012B-Q-59	08	B600_G5323	—	5600, 5700	2000
SPT-CL J0406-4805	04:06:54.6	-48:05:11	8.13	GS-2013B-Q-72	09	R400_G5325	GG455_G0329	6500, 6600	2500
				GS-2013B-Q-72	10	R400_G5325	GG455_G0329	6500, 6600	2500
SPT-CL J0411-4819	04:11:15.7	-48:19:18	15.26	GS-2012B-Q-59	15	B600_G5323	—	5600, 5700	2200
				GS-2012B-Q-59	16	B600_G5323	—	5600, 5700	2400
SPT-CL J0417-4748	04:17:22.8	-47:48:50	14.24	GS-2012B-Q-29	11	R400_G5325	GG455_G0329	6600, 6700	3600
				GS-2012B-Q-29	12	R400_G5325	GG455_G0329	6600, 6700	3600
SPT-CL J0426-5455	04:26:04.8	-54:55:10	8.85	GS-2013B-Q-25	14	R400_G5325	GG455_G0329	7000, 7100	5760
SPT-CL J0438-5419	04:38:18.0	-54:19:16	22.88	GS-2011A-C-03	28	R400_G5325	GG455_G0329	5500, 5550	2700
SPT-CL J0456-5116	04:56:27.9	-51:16:36	8.58	GS-2013B-Q-25	17	R400_G5325	GG455_G0329	7000, 7100	4200
				GS-2013B-Q-25	18	R400_G5325	GG455_G0329	7000, 7100	4200
SPT-CL J0511-5154	05:11:41.0	-51:54:15	7.09	GS-2011B-C-06	58	R400_G5325	GG455_G0329	6600, 6650	4800
				GS-2011B-C-06	59	R400_G5325	GG455_G0329	6600, 6650	4800
SPT-CL J0539-5744	05:40:01.0	-57:44:25	6.74	GS-2012B-Q-29	17	R400_G5325	GG455_G0329	7100, 7200	4800
				GS-2012B-Q-29	18	R400_G5325	GG455_G0329	7100, 7200	4800
SPT-CL J0542-4100	05:42:52.0	-41:00:15	7.92	GS-2013B-Q-25	19	R400_G5325	GG455_G0329	7000, 7100	4800
				GS-2013B-Q-25	20	R400_G5325	GG455_G0329	7000, 7100	4800
SPT-CL J0549-6205	05:49:20.2	-62:05:08	25.81	GS-2012B-Q-59	09	B600_G5323	—	5500, 5600	1800
				GS-2012B-Q-59	10	B600_G5323	—	5500, 5600	1800
SPT-CL J0555-6406	05:55:27.9	-64:06:11	12.72	GS-2012B-Q-59	11	B600_G5323	—	5600, 5700	2000
				GS-2012B-Q-59	12	B600_G5323	—	5600, 5700	2000
SPT-CL J0655-5234	06:55:51.0	-52:34:03	7.76	GS-2013B-Q-72	15	R400_G5325	GG455_G0329	6400, 6500	2600
				GS-2013B-Q-72	16	R400_G5325	GG455_G0329	6400, 6500	2600
SPT-CL J2017-6258	20:17:56.1	-62:58:41	6.32	GS-2013B-Q-72	01	R400_G5325	GG455_G0329	6500, 6600	2800
				GS-2013B-Q-72	02	R400_G5325	GG455_G0329	6500, 6600	2800
SPT-CL J2020-6314	20:20:06.6	-63:14:36	5.38	GS-2012A-Q-37	09	R400_G5325	GG455_G0329	6600, 6700	3600
				GS-2012A-Q-37	10	R400_G5325	GG455_G0329	6600, 6700	3600
SPT-CL J2026-4513	20:26:27.5	-45:13:36	5.24	GS-2013B-Q-25	01	R400_G5325	GG455_G0329	7000, 7100	5760
				GS-2014B-Q-64	03	R400_G5325	GG455_G0329	7200, 7300	4800
SPT-CL J2030-5638	20:30:48.9	-56:38:10	5.50	GS-2013B-Q-72	03	B600_G5323	—	5800, 5900	2000
				GS-2013B-Q-72	04	B600_G5323	—	5800, 5900	2000
				GS-2012A-Q-04	01	B600_G5323	—	5400, 5500	2000
				GS-2012A-Q-04	02	B600_G5323	—	5400, 5500	2000

TABLE 1 — *Continued*

Cluster	RA	Dec	ξ_{SPT}	Program ID	Mask	Grating	Filter	λ_c (Å)	t_{exp} (s)
SPT-CL J2035-5251	20:35:12.3	-52:51:06	9.71	GS-2013A-Q-45	01	B600_G5323	—	5600, 5700	3900
				GS-2013A-Q-45	02	B600_G5323	—	5600, 5700	2600
SPT-CL J2058-5608	20:58:21.1	-56:08:43	5.01	GS-2011A-C-03	03	R400_G5325	GG455_G0329	5500, 5550	3000
				GS-2011A-C-03	04	R400_G5325	GG455_G0329	5500, 5550	3000
SPT-CL J2115-4659	21:15:12.3	-46:59:27	5.18	GS-2012A-Q-37	03	B600_G5323	—	5200, 5300	2000
				GS-2012A-Q-37	04	B600_G5323	—	5200, 5300	2000
SPT-CL J2118-5055	21:18:55.6	-50:55:56	5.54	GS-2012A-Q-04	09	R400_G5325	GG455_G0329	6600, 6700	4800
				GS-2011B-C-06	50	R400_G5325	GG455_G0329	6600, 6650	4320
SPT-CL J2136-4704	21:36:28.6	-47:04:54	6.24	GS-2011A-C-03	21	R400_G5325	GG455_G0329	5500, 5550	3000
				GS-2011A-C-03	22	R400_G5325	GG455_G0329	5500, 5550	3000
SPT-CL J2140-5727	21:40:33.4	-57:27:27	5.35	GS-2012A-Q-37	05	B600_G5323	—	5600, 5700	2800
				GS-2012A-Q-37	06	B600_G5323	—	5600, 5700	2800
SPT-CL J2146-4846	21:46:07.4	-48:46:48	5.96	GS-2011A-C-03	31	R400_G5325	GG455_G0329	5500, 5550	4200
				GS-2011A-C-03	32	R400_G5325	GG455_G0329	5500, 5550	4200
SPT-CL J2146-5736	21:46:47.0	-57:36:53	6.19	GS-2012A-Q-04	03	R400_G5325	GG455_G0329	6600, 6700	4400
				GS-2012A-Q-04	04	R400_G5325	GG455_G0329	6600, 6700	4400
SPT-CL J2155-6048	21:55:56.4	-60:48:27	5.74	GS-2011A-C-03	17	R400_G5325	GG455_G0329	5500, 5550	2700
				GS-2011A-C-03	18	R400_G5325	GG455_G0329	5500, 5550	2700
SPT-CL J2159-6244	21:59:57.9	-62:44:29	6.49	GS-2012A-Q-37	07	B600_G5323	—	5600, 5700	2600
				GS-2012A-Q-37	08	B600_G5323	—	5600, 5700	2600
SPT-CL J2218-4519	22:19:00.0	-45:19:11	5.54	GS-2013B-Q-25	07	R400_G5325	GG455_G0329	6900, 7000	3200
SPT-CL J2222-4834	22:22:50.9	-48:34:24	9.08	GS-2012A-Q-04	12	R400_G5325	GG455_G0329	6600, 6700	4800
				GS-2012A-Q-04	13	R400_G5325	GG455_G0329	6600, 6700	4800
SPT-CL J2232-5959	22:32:35.7	-59:59:25	8.80	GS-2012A-Q-04	05	R400_G5325	GG455_G0329	6600, 6700	4000
				GS-2012A-Q-04	06	R400_G5325	GG455_G0329	6600, 6700	4000
SPT-CL J2233-5339	22:33:19.1	-53:39:00	8.29	GS-2012A-Q-37	11	B600_G5323	—	5600, 5700	2800
				GS-2012A-Q-37	12	B600_G5323	—	5600, 5700	2800
SPT-CL J2245-6206	22:45:41.4	-62:02:38	8.74	GS-2012A-Q-04	07	R400_G5325	GG455_G0329	6700, 6800	3000
				GS-2012A-Q-04	08	R400_G5325	GG455_G0329	6700, 6800	3000
SPT-CL J2258-4044	22:58:49.2	-40:44:19	10.95	GS-2014B-Q-31	05	R400_G5325	GG515_G0330	7600, 7700	4400
				GS-2014B-Q-31	06	R400_G5325	GG515_G0330	7600, 7700	4400
SPT-CL J2301-4023	23:01:51.2	-40:23:16	8.09	GS-2014B-Q-64	04	R400_G5325	GG455_G0329	7200, 7300	4800
				GS-2014B-Q-64	05	R400_G5325	GG455_G0329	7200, 7300	4800
SPT-CL J2306-6505	23:06:55.1	-65:05:27	9.22	GS-2012A-Q-37	13	R400_G5325	GG455_G0329	6600, 6700	5400
				GS-2012A-Q-37	14	R400_G5325	GG455_G0329	6600, 6700	3600
SPT-CL J2325-4111	23:25:13.0	-41:11:45	12.50	GS-2011A-C-03	25	B600_G5323	—	5200, 5250	1800
				GS-2011A-C-03	26	B600_G5323	—	5200, 5250	1800
SPT-CL J2335-4544	23:35:08.7	-45:44:19	10.37	GS-2013B-Q-72	05	R400_G5325	GG455_G0329	6500, 6600	2800
				GS-2013B-Q-72	06	R400_G5325	GG455_G0329	6500, 6600	2800
SPT-CL J2344-4243	23:44:44.3	-42:43:15	27.44	GS-2011A-C-03	29	R400_G5325	GG455_G0329	5500, 5550	4200
				GS-2011A-C-03	30	R400_G5325	GG455_G0329	5500, 5550	4200

NOTE. — This table summarizes the SPT-GMOS observations for each individual spectroscopic mask that was observed. The columns report, from left to right, the cluster name, cluster coordinates, Gemini program ID, the mask number within the Gemini program, the grating used, the order-sorting filter used (if any), the central wavelengths used for individual spectroscopic exposures, and the total integration time for which the mask was exposed.

a There is not a reliable SZ measurement available for this cluster due to a nearby mm-bright point source.

2.3.2. *Instrumental Setup*

Our observations are divided broadly into two groups: one using the B600_G5323 grating with no filter, and one using the R400_G5325 grating with the GG455_G0329 long-pass filter. The decision of which grating to use was made based on the best-available photometric redshift estimate of each cluster (e.g., Song et al. 2012; Bleem et al. 2015), where clusters with $z_{phot} \leq 0.45$ were observed with the B600_G5323 grating, and those having $z_{phot} > 0.45$ with the R400_G5325 grating; this division was chosen to ensure that each cluster field was observed using a grating that has optimal throughput in the wave-

length range where important spectral features appear at each approximate cluster redshift.

The primary features of interest include [O II] $\lambda3727,3729$ (hereafter [O II] $\lambda3727$), Ca H&K, the Franhaufer G-band (a complex of Ca and Fe lines), the Balmer break, and the n = 6 $\longleftrightarrow$ 2 (hereafter H-δ), n = 5 $\longleftrightarrow$ 2 (hereafter H-γ), and n = 4 $\longleftrightarrow$ 2 (hereafter H-β) hydrogen Balmer lines. Central wavelengths were chosen to disperse spectra such that λ = 4300Å would fall approximately in the middle of the detector for a slit placed near the middle of the GMOS-South focal plane. We binned the detector by a factor of two in the spectral/dispersion direction for all observations. We generally left the detector unbinned along the spatial direction (i.e., along the slit) to provide the best-possible sampling along the slits, though some early observations were binned by a factor of two along the spatial direction.

The sole exception to these standard setups were the observations of SPT-CL J0243-4833, which used the
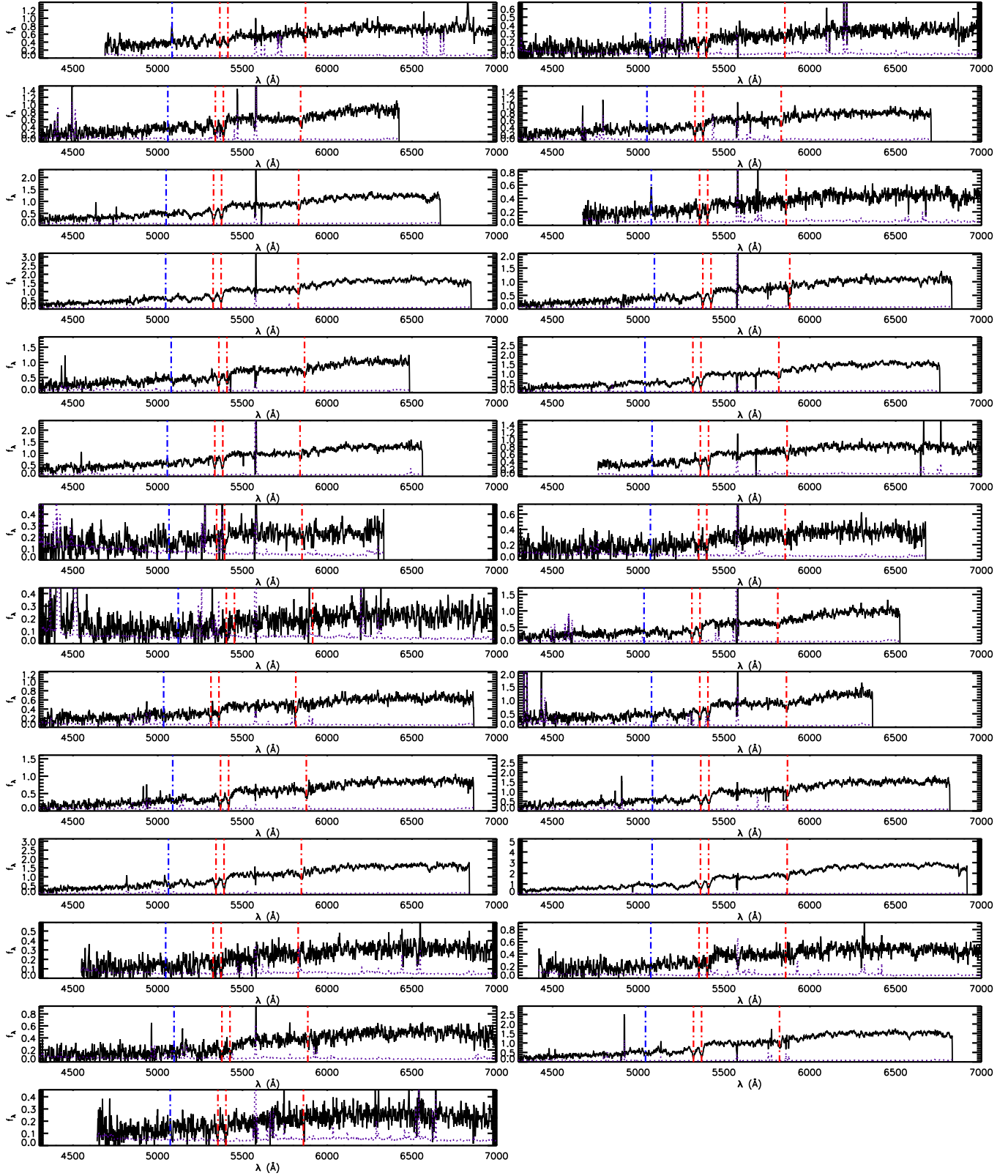
FIG. 2.— Final 1-dimensional spectra for all 27 SPT-GMOS galaxies that we classify as cluster members of SPT-CL J0348-4515 at $z = 0.3592$, a galaxy cluster near the lower redshift range of clusters targeted in SPT-GMOS. These are example data taken in standard MOS mode. Each panel contains the spectrum for a single galaxy, all of which are plotted as a function of the observed/instrumental wavelength over a common wavelength interval ($\Delta\lambda = 4300 - 7000$), with the uncertainty per pixel over-plotted as a purple dotted line. In each panel we also over-plot three vertical dot-dashed lines that indicate the locations of [O II] $\lambda3727$ in emission (blue), as well as Ca II H & K and G-Band in absorption (red) at the spectroscopic redshift measured for that galaxy. Along with Figure 3, these data demonstrate the typical range in S/N of SPT-GMOS cluster galaxy spectra.

R400_G5325 grating *without* a long-pass order-sorting filter. This was an experimental setup that was used to evaluate the benefits of observing without the filter, which imposes an additional ~5-10% throughput loss, and relying on the throughput curve of the R400_G5325 grating to serve a similar purpose to the long-pass filter. This setup was not used regularly because of the additional difficulties that it imposed on wavelength calibrations that result from second order images of arc lamp emission lines.

Grating, filter, and central wavelength choices for all cluster observations are listed in Table 1. The consistent slit widths and instrumental setups used for our observations result in spectra that all have similar spectral resolutions and corresponding resolving powers, $d\lambda \simeq 7 - 9$Å and $R \simeq 600 - 1000$, respectively. We chose the total spectroscopic integration times (see Table 1) to match the prediction from the GMOS-South integration time calculator[52] for the time necessary to obtain a signal-to-noise $(S/N) = 5$ per spectral element immediately blueward of the 4000Å break for a typical $m^\star + 1$ passive galaxy at the redshift of each cluster.

2.3.3. *Micro Nod-and-shuffle Multi-object Spectroscopy*

Due to the poor GMOS-South *e2v* detector performance at redder wavelengths we observed galaxy clusters with photometric redshift estimates $z_{phot} \geq 0.65$ in "microscopic" nod-and-shuffle (N&S) mode. This mode uses very short slitlets — between 3-4″ in length in our observations — such that the target source can be placed on one half of the slitlet with the other half collecting blank sky. The telescope is then nodded back and forth on the sky to move the target sources between the two halves of the slitlets, while the charge on the detector is shuffled in concert with each telescope nod. The resulting 2D detector image contains two separate traces (A and B) for each slitlet — one with the target source at each end of the slitlet. A difference of the two traces resulting from each individual slitlet yields two sky-subtracted traces for the target source (one positive, one negative).

The advantage of this mode of observation is that the nod cycle can be performed on relatively short timescales to match the timescale on which the intensity of sky emission varies — typically a few minutes. The sky-subtraction results in nearly Poisson noise statistics. Each pair of slitlet traces contain complementary pairs of source+sky and sky-only spectra such that the source+sky spectrum from trace A was observed through the identical optical path (instrument and telescope) as the complementary trace B sky-only spectrum, and vice versa. We used a nod cycle time of 120s (i.e., one 120s interval spent integrating at each of position A and position B in a single nod cycle), and repeated a number of nod cycles split across two or three science exposures to reach the required total integration times described in Section 2.3.2.

2.3.4. *Mask Design*

Optical and infrared imaging observations of the 2500 deg² SPT cluster candidates are available from an extensive multi-facility campaign to identify red-sequence galaxy populations at the position of each candidate. These data are discussed in detail in previous SPT collaboration papers (High et al. 2010; Song et al. 2012; Bleem et al. 2015), and we refer the reader to those publications for more information.

The pre-existing follow-up confirmation imaging is sufficient in most cases to produce photometric catalogs of candidate red-sequence cluster member galaxies down to at least $m^\star + 1$, which is sufficient for designing masks for SPT-GMOS spectroscopy. For those SPT-SZ galaxy clusters that did not have follow-up imaging sufficient to reach $m^\star + 1$ depths we obtained additional pre-imaging with Gemini/GMOS-South. Pre-imaging observations were performed in two bands, chosen to span the 4000Å break (either gr, or ri), with integration times chosen to achieve 10σ depth for a galaxy of $m^\star + 1$ at the best-available estimate of the cluster photometric redshift. The GMOS pre-imaging data were reduced using the standard scripts from the Gemini/GMOS IRAF package[53]; these scripts subtract off the bias level for each GMOS detector, apply a flat-field correction using observations of a flat lamp-illuminated source within the Gemini-South dome, and map the three individual GMOS detectors onto a single mosaicked image using geometric transformations provided by the Gemini Observatory. We photometrically calibrate the pre-imaging using unsaturated stars that appear within the field of view of both the GMOS and pre-existing follow-up imaging.

All masks were designed with the Gemini MOS Mask Preparation Software (GMMPS) tool, which can use either native GMOS pre-imaging or "pseudo-pre-imaging" generated from optical imaging from other facilities. We designed two spectroscopic masks for each cluster using a single input catalog. GMMPS takes an input catalog and generates one or more spectroscopic masks with slits placed based on three discrete tiers of priority. For each cluster we used the highest priority to target the galaxy or galaxies that were identified as likely candidates to be the brightest cluster galaxy (BCG), and also occasionally to target other objects of special interest such as bright giant arcs resulting from strong gravitational lensing. The next highest priority was used to target candidate cluster member galaxies that were selected from the red sequence, which we identified as an overdensity in color-magnitude (e.g., $g-r$ vs r) and color-color space (e.g., $g - r$ vs $r - z$). The lowest priority tier included all galaxies that were potentially drawn from the "blue cloud" population of cluster galaxies, which we selected as all galaxies that were bluer than the red sequence and not obviously in the foreground (i.e., not brighter than the brightest end of the main sequence).

Masks were designed with slit lengths for standard multi-object masks varying between 6-8″ in length depending on the typical sizes of the galaxies being observed, where the galaxies in lower redshift clusters have larger angular sizes than those in higher redshift clusters. For the large majority of our standard MOS masks we used slits with lengths between 6-6.5″. Slitlet lengths on the N&S masks (targeting the higher redshift clusters) varied between 3.1-4″, with the majority using 3.5″

---

[52]   http://www.gemini.edu/sciops/instruments/integration-time-calculators/gmoss-itc

[53] https://www.gemini.edu/node/11823
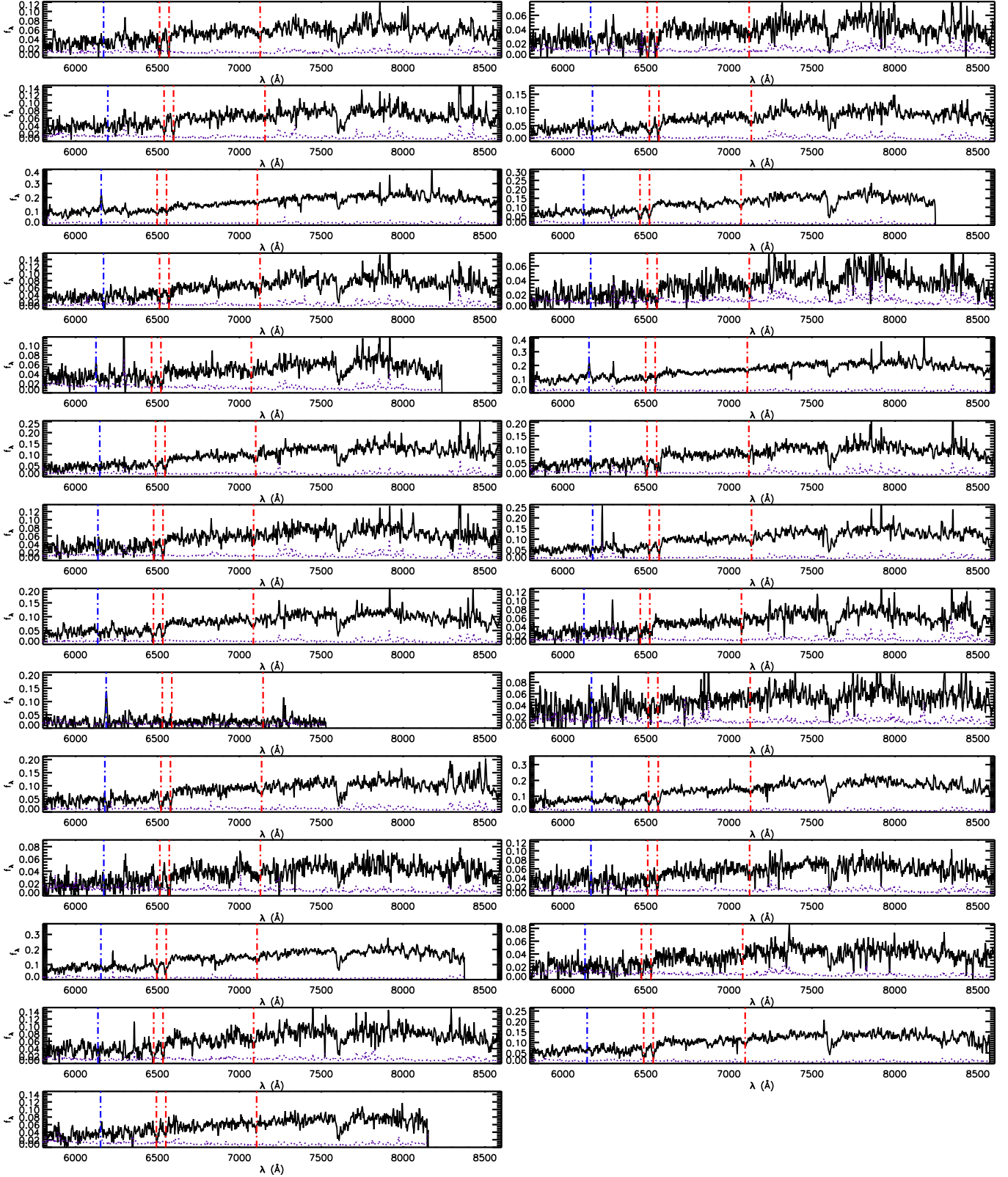
FIG. 3.— Final 1-dimensional spectra for all 27 SPT-GMOS galaxies that we classify as cluster members of SPT-CL J2222-4834 at $z = 0.6519$, a galaxy cluster near the upper redshift range of clusters targeted in SPT-GMOS. These are example data taken in N&S mode. Each panel contains the spectrum for a single galaxy, all of which are plotted as a function of the observed/instrumental wavelength over a common wavelength interval ($\Delta\lambda = 6200 - 8800$), with the uncertainty per pixel over-plotted as a purple dotted line. In each panel we also over-plot three vertical dot-dashed lines that locations of [O II] $\lambda3727$ in emission (blue), as well as Ca II H & K and G-Band in absorption (red) at the spectroscopic redshift measured for that galaxy. Along with Figure 2, these data demonstrate the typical range in S/N of SPT-GMOS cluster galaxy spectra.

$\langle \delta z/(1+z) \rangle = 0.015$
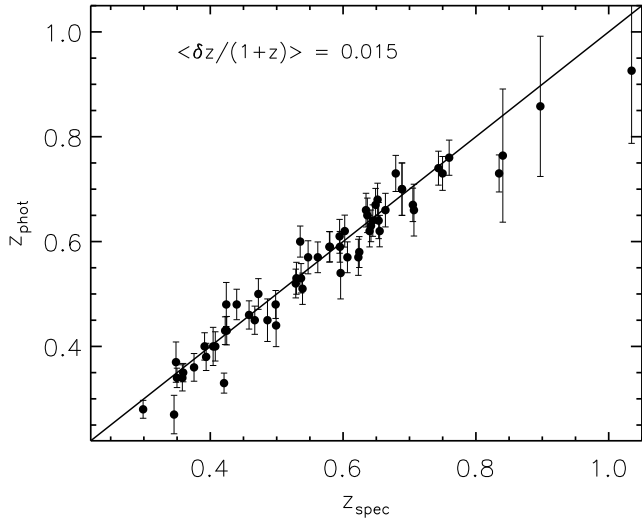
FIG. 4.— Spectroscopic vs. photometric redshifts for the 62 SPT-GMOS clusters presented here, using photo-z's described in Bleem et al. (2015), with the scatter between the two $\sim 1.5\%$. SPT-GMOS spectroscopy provides a strong anchor for the photometric redshift calibration at low to intermediate redshift.

lengths as we found this to be a good balance between optimizing the N&S subtraction and maximizing the number of slitlets placed on each mask. The standard slit width for all masks was $1''$, which is a good match to the typical size of the fainter galaxies that we targeted, and therefore strikes a balance between throughput and spectral resolution. Individual standard (N&S) multi-object masks typically contain $\sim$30-40 (30-35) slits, with approximately one half to two thirds of those slits generally being placed on galaxies with a high probability of being cluster members. The slight difference in slit-packing between standard vs. N&S modes simply reflects the fact that N&S slits effectively take up twice their length in available detector space, and our most commonly used N&S slit length is slightly greater than 1/2 our most commonly used standard MOS slit length.

3. SPECTROSCOPIC DATA REDUCTION

We reduced all SPT-GMOS spectroscopic data uniformly using a custom pipeline. The pipeline relies primarily on scripts from the Gemini IRAF package[54] developed by Gemini Observatory. We supplement the Gemini IRAF scripts with our own custom code — described in more detail below — that is based on the XIDL[55] package. Some elements of the reduction pipeline vary slightly across the spectroscopic dataset, reflecting differences in the observing strategy — standard multi-object spectroscopy vs nod-and-shuffle — and differences in the GMOS-South detectors before and after the 2014B semester. Below we describe the reduction process for each detector and each observing mode.

3.1. *GMOS-South Spectra with e2v Detectors*
3.1.1. *Standard Multi-object Spectroscopy*

The majority of our spectroscopic observations are standard multi-object spectroscopy, and we use standard

[54] https://www.gemini.edu/node/10795/
[55] http://www.ucolick.org/~xavier/IDL/

Gemini IRAF scripts to reduce these data. For the majority of the spectroscopic masks we take both arc lamp frames for wavelength calibration and quartz lamp flat-field frames interspersed between science frames, on sky, to ensure as little instrumental variation as possible between calibration and science frames. In a few cases — primarily observations conducted in classical mode and already published in Ruel et al. (2014) — we use day-time arc lamp frames and rely on sky lines in the science exposures to refine the wavelength calibration.

Our pipeline begins by subtracting a master bias frame from the science, arc lamp, and flat-field calibration frames. We then use the flat-field frames to identify the trace of each individual slit and to derive a flat-field correction. We then reduce and extract the 2D spectrum associated with each individual slit on the mask for both the science and arc lamp calibration frames. The extracted 2D arc lamp spectra are then used to fit a wavelength calibration for each slit using the standard line lists provided by Gemini Observatory, typically using 20-30 arc lamp lines per slit, depending on the wavelength coverage of each slit. The wavelength solutions are applied to the science spectra, which are then used to fit a sky model that excludes the source trace and assumes a constant sky spectrum along the length of the slit. We subtract the sky model for each slit and apply cosmic ray rejection to each individual sky-subtracted 2D spectrum using a modified version of LACOSMIC (van Dokkum 2001). We then use custom IDL[56] scripts to fit the source trace in each slit and extract a single 1D spectrum from each 2D science exposure. All of the 1D extractions for a given slit on a given mask are then combined using the XIDL "long_combine" procedure.

We generate approximate flux calibrations in each of the instrumental configurations using archival "partner" observations of southern spectrophotometric standard stars. Specifically, we reduced archival data for the standards LTT1788, LTT7379 (Hamuy et al. 1992, 1994), and G158-100 (Oke 1990) using the standard Gemini IRAF scripts to generate average flux calibrations for GMOS-South in the configurations used for our science spectra. We apply these average flux calibrations to our science spectra, resulting in final source spectra that are "flattened" to correct for the relative throughput as a function of wavelength, but do not provide a reliable absolute zero point flux calibration.

3.1.2. *Micro N&S Multi-object Spectroscopy*

Reduction of N&S spectra differs somewhat from standard MOS data, in large part because the sky-subtraction step is best performed early in the process. We begin with these data by applying a standard bias subtraction to all frames. We then use custom IDL code based on previous work reducing N&S spectra from GMOS-North (Bayliss et al. 2011b) to create a master dark frame from day-time calibration exposures that reproduce the exposure times and charge shuffle patterns used in our science frames. The dark calibration serves primarily to identify and mask out regions of the detector that act as "charge traps" when charge is shuffled up and down along detector columns.

[56] http://www.exelisvis.co.uk/ProductsServices/IDL.aspx

TABLE 2
Spectroscopy of SPT Clusters: Results

Cluster Name	N_{spec}	$N_{members}$	$\bar{z}_{cluster}$	$\sigma_{v,BI}$ (km s^{-1})	$\sigma_{v,G}$ (km s^{-1})	A^{2*}	α_{AD}
SPT-CL J0013-4906	51	41	0.4075 ± 0.0052	1103 ± 160	1105 ± 160	0.481	0.23599
SPT-CL J0033-6326	45	18	0.5963 ± 0.0102	1916 ± 427	1941 ± 433	0.264	0.81568
SPT-CL J0040-4407[a]	44	36	0.3498 ± 0.0057	1259 ± 195	1276 ± 198	0.238	0.94321
SPT-CL J0102-4603	48	20	0.8405 ± 0.0050	807 ± 170	803 ± 169	0.533	0.17476
SPT-CL J0106-5943	50	29	0.3484 ± 0.0058	1298 ± 225	1304 ± 226	0.390	0.39682
SPT-CL J0118-5156[a]	23	14	0.7051 ± 0.0053	934 ± 238	949 ± 242	0.559	0.15117
SPT-CL J0123-4821	31	20	0.6550 ± 0.0083	1505 ± 317	1490 ± 314	0.568	0.14325
SPT-CL J0142-5032	45	31	0.6793 ± 0.0056	1000 ± 168	1006 ± 169	0.253	0.86765
SPT-CL J0200-4852	58	35	0.4991 ± 0.0040	796 ± 125	803 ± 126	0.191	0.76500
SPT-CL J0205-6432[a]	24	15	0.7436 ± 0.0042	714 ± 175	683 ± 168	0.912	0.02010
SPT-CL J0212-4656[a]	40	26	0.6535 ± 0.0051	931 ± 171	921 ± 169	0.723	0.05919
SPT-CL J0233-5819[a]	11	10	0.6638 ± 0.0042	754 ± 231	781 ± 239	0.361	0.46679
SPT-CL J0243-4833	44	39	0.4984 ± 0.0065	1293 ± 193	1329 ± 198	1.004	0.01184
SPT-CL J0243-5930	44	26	0.6345 ± 0.0053	975 ± 179	978 ± 180	0.296	0.67867
SPT-CL J0245-5302[a]	38	29	0.3000 ± 0.0055	1262 ± 219	1260 ± 219	0.267	0.80064
SPT-CL J0252-4824	42	24	0.4207 ± 0.0030	635 ± 121	656 ± 126	0.441	0.29543
SPT-CL J0304-4401	48	35	0.4584 ± 0.0054	1114 ± 175	1116 ± 176	0.479	0.23764
SPT-CL J0307-6225	36	20	0.5801 ± 0.0034	652 ± 137	618 ± 130	1.071	0.00808
SPT-CL J0310-4647	45	28	0.7067 ± 0.0035	617 ± 109	628 ± 111	0.515	0.19385
SPT-CL J0324-6236	33	10	0.7498 ± 0.0032	546 ± 167	520 ± 159	0.904	0.02096
SPT-CL J0334-4659	51	34	0.4861 ± 0.0061	1223 ± 195	1203 ± 192	0.907	0.02062
SPT-CL J0348-4515	41	27	0.3592 ± 0.0057	1246 ± 224	1255 ± 226	0.277	0.75715
SPT-CL J0352-5647	33	17	0.6490 ± 0.0045	813 ± 186	812 ± 186	0.509	0.20113
SPT-CL J0356-5337	36	8	1.0345 ± 0.0112	1647 ± 572	1691 ± 588	0.279	0.74516
SPT-CL J0403-5719	52	29	0.4670 ± 0.0048	990 ± 172	1008 ± 175	0.484	0.23170
SPT-CL J0406-4804	33	27	0.7355 ± 0.0070	1216 ± 219	1216 ± 219	0.503	0.20804
SPT-CL J0411-4819	54	44	0.4241 ± 0.0060	1267 ± 177	1294 ± 181	0.381	0.41758
SPT-CL J0417-4748	49	32	0.5794 ± 0.0060	1133 ± 187	1139 ± 188	0.359	0.47270
SPT-CL J0426-5455	17	11	0.6420 ± 0.0050	910 ± 265	950 ± 276	0.247	0.89796
SPT-CL J0438-5419[a]	23	17	0.4224 ± 0.0069	1448 ± 333	1481 ± 340	0.246	0.90123
SPT-CL J0456-5116	45	23	0.5619 ± 0.0043	821 ± 161	804 ± 157	0.566	0.14491
SPT-CL J0511-5154[a]	23	15	0.6447 ± 0.0042	758 ± 186	779 ± 191	0.356	0.48046
SPT-CL J0539-5744	44	19	0.7597 ± 0.0063	1075 ± 233	1118 ± 242	0.316	0.60336
SPT-CL J0542-4100	44	31	0.6399 ± 0.0056	1031 ± 173	1036 ± 174	0.229	0.99178
SPT-CL J0549-6205	47	27	0.3755 ± 0.0027	666 ± 120	669 ± 120	0.197	0.81417
SPT-CL J0555-6406	53	31	0.3455 ± 0.0049	1088 ± 182	1073 ± 180	0.617	0.10821
SPT-CL J0655-5234	50	30	0.4724 ± 0.0043	883 ± 150	902 ± 154	0.258	0.84035
SPT-CL J2017-6258	54	37	0.5354 ± 0.0050	972 ± 149	961 ± 147	0.315	0.60867
SPT-CL J2020-6314	43	18	0.5367 ± 0.0050	891 ± 198	890 ± 198	0.506	0.20410
SPT-CL J2026-4513	47	19	0.6887 ± 0.0067	1182 ± 256	1227 ± 266	0.232	0.97541
SPT-CL J2030-5638	67	39	0.3937 ± 0.0029	619 ± 92	631 ± 94	0.180	0.72546
SPT-CL J2035-5251	61	32	0.5287 ± 0.0052	1015 ± 167	1022 ± 168	0.271	0.78107
SPT-CL J2058-5608[a]	16	9	0.6065 ± 0.0056	1038 ± 337	990 ± 322	2.185	0.00001
SPT-CL J2115-4659	43	29	0.2989 ± 0.0040	934 ± 162	943 ± 164	0.150	0.76338
SPT-CL J2118-5055[a,b]	30	13	0.6244 ± 0.0056	1035 ± 274	1088 ± 289	0.208	0.79140
SPT-CL J2136-4704[a]	28	24	0.4247 ± 0.0069	1448 ± 277	1461 ± 280	0.364	0.45986
SPT-CL J2140-5727	47	17	0.4043 ± 0.0056	1192 ± 274	1176 ± 270	0.375	0.43196
SPT-CL J2146-4846[a]	29	26	0.6230 ± 0.0042	768 ± 141	771 ± 141	0.285	0.72234
SPT-CL J2146-5736	51	25	0.6025 ± 0.0050	936 ± 175	942 ± 177	0.264	0.81491
SPT-CL J2155-6048[a]	31	24	0.5389 ± 0.0054	1049 ± 201	1079 ± 207	0.323	0.58092
SPT-CL J2159-6244	53	41	0.3914 ± 0.0034	723 ± 105	725 ± 105	0.204	0.75778
SPT-CL J2218-4519	24	20	0.6365 ± 0.0064	1172 ± 247	1207 ± 254	0.456	0.27124
SPT-CL J2222-4834	46	27	0.6519 ± 0.0055	1002 ± 180	1002 ± 180	0.499	0.21291
SPT-CL J2232-5959	46	26	0.5948 ± 0.0053	1004 ± 184	1008 ± 185	0.251	0.87831
SPT-CL J2233-5339	45	31	0.4398 ± 0.0050	1045 ± 175	975 ± 163	0.839	0.03045
SPT-CL J2245-6206	46	4	0.5856 ± 0.0072	1363 ± 724	1406 ± 747	0.550	0.15872
SPT-CL J2258-4044	44	27	0.8971 ± 0.0077	1220 ± 220	1248 ± 225	0.322	0.58278
SPT-CL J2301-4023	55	20	0.8349 ± 0.0063	1023 ± 216	1045 ± 220	0.911	0.02013
SPT-CL J2306-6505	57	43	0.5297 ± 0.0058	1132 ± 160	1138 ± 161	0.188	0.91693
SPT-CL J2325-4111[a]	47	33	0.3579 ± 0.0088	1932 ± 314	1926 ± 313	0.342	0.52026
SPT-CL J2335-4544	46	35	0.5473 ± 0.0050	974 ± 153	948 ± 149	1.343	0.00171
SPT-CL J2344-4243[a]	42	32	0.5952 ± 0.0097	1814 ± 299	1825 ± 301	0.167	0.79178

Note. — A summary of the results of SPT-GMOS spectroscopy by galaxy cluster. Columns from left to right report the cluster name, the total number of spectra with radial velocity measurements, the number of cluster member galaxies, the median cluster redshift, the velocity dispersion estimates (using the bi-weight and gapper estimators) for each observed SPT cluster, the value of the AD test statistic, and the probability that the observed cluster velocities were drawn from a Gaussian velocity distribution.

[a] Cluster also presented in Ruel et al. (2014).

[b] Numbers here are computed from SPT-GMOS data only, but are fully consistent with the results combining these data with spectra from other facilities in Ruel et al. (2014).
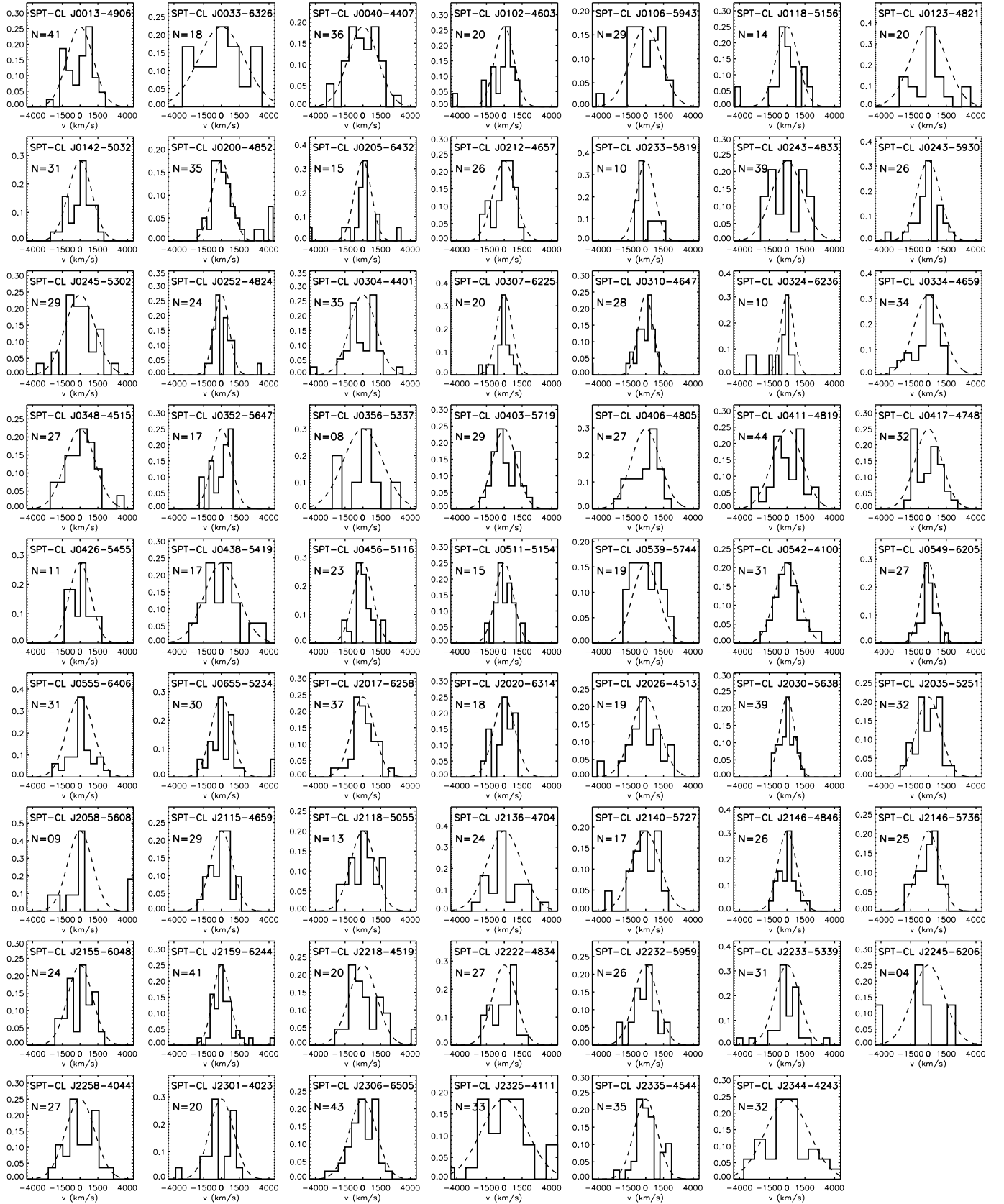
FIG. 5.— Velocity distributions for the 62 galaxy clusters in the SPT-GMOS survey program. Over-plotted as dashed lines are Gaussian distributions with centers and widths matching the bi-weight estimates of the median and dispersion for each galaxy cluster. The velocities plotted here for each cluster have been converted to peculiar velocities relative to the bi-weight estimate of the median recession velocity for each galaxy cluster. The number of members used to estimate the dispersion of each cluster is indicated in each panel.

For N&S spectra the sky subtraction step is trivially achieved by differencing each science frame from itself, offset along the columns of the CCD by the shuffle distance. This step results in two 2D sky-subtracted spectral traces for each slit, one positive and the other negative, corresponding to the spectra dispersed at both of the original pointed position and the nodded-to position, respectively. The sky-subtracted spectra are reduced using standard Gemini IRAF routines to apply a flat-field calibration and wavelength solution, and we apply the same custom IDL routines to extract a separate 1D spectrum from each 2D spectral trace — i.e., each science exposure produces two 1D extractions. We combine all 1D spectra from each slit and apply flux calibrations identically to the standard MOS spectra described above.

3.2. GMOS-South Spectra with Hamamatsu Detectors

Gemini Observatory upgraded the GMOS-South detector in 2014B, replacing the old *e2v* CCD chips with Hamamatsu chips. The SPT-GMOS survey observations were primarily conducted prior to 2014B, but SPT-GMOS observations performed between Dec 2014 and Dec 2015 used the upgraded detectors. These new chips provide a tremendous improvement in the sensitivity of the instrument, improving the quantum efficiency by more than a factor of two redward of $\sim$8000Å, and by approximately an order of magnitude at $\sim$10000Å. The Hamamatsu chips are also much less prone to fringing and it is therefore not necessary to rely on N&S observations to obtain high-quality spectra at redder wavelengths. The increased performance of these new detectors does come at the cost of a much higher cosmic ray hit-rate per detector pixel, such that shorter individual exposures ($t_{exp} \lesssim$ 1200s) are strongly recommended. In masks designed for the Hamamatsu detectors we experimented with different exposure-splitting strategies, acquiring up to six individual science exposures with each mask (vs. the two-exposure strategy that we used for spectra taken with the older detectors) with the goal of improving cosmic ray rejection for Hamamatsu spectra.

The reduction pipeline for spectra with the Hamamatsu detectors is almost identical to the process applied to the older *e2v* detectors, with the notable exception of cosmic ray rejection. The shorter individual spectroscopic exposures ($\lesssim$ 1200s) also result in very faint traces for spectra from the typical cluster member galaxies at $z \gtrsim 0.8$, which introduces potential problems with the extraction of 1D spectra from individual 2D spectral images. Our reduction pipeline for the *e2v* spectra — described above — is not necessarily optimal for the new Hamamatsu spectra. Specifically, the high rate of cosmic ray hits and shorter individual exposure times raise concerns about the single-image cosmic ray rejection and 1D extraction algorithms that we apply to each individual *e2v* science frame.

We have experimented with two different reduction schemes, one identical to the procedure applied to data taken with the old detectors, and a second in which we perform cosmic ray rejection simultaneously while stacking pairs of individual sky-subtracted 2D science spectra, slit by slit for each mask, applying the IRAF CRREJECT algorithm. This second method results in half as many clean 2D spectra for each mask slit — which we

trace, extract, and combine using the same custom IDL code described above. Careful work with the final spectra that result from each reduction method does not clearly favor one method as universally better; the final spectra resulting from the first method (the one applied to old detector data) are often high quality, and this method has the general advantage of producing a final S/N-weighted stack of individual 1D exposures, which allows us to make optimal use of different 2D spectra exposures where the average seeing (and thus the profile of the spectral trace) is varying between exposures. However, there are some cases where the second method using stacks of 2D spectra generates a final spectrum that is cleaner with better S/N than the first method. We generate reductions for all Hamamatsu spectra using both methods, and measure as many redshifts as possible from the two reductions. The "best" reduction method seems to vary across different masks and slits, and at this time we conclude that the best practices for reducing spectra taken with the new Hamamatsu detectors are still an open question.

Our spectra taken with the Hamamatsu detectors do suffer from the effects of a malfunction involving amplifier #5. Some or all of the columns read out by this amplifier are occasionally and unpredictably "hot", such that the data recorded there are lost. This problem was diagnosed by Gemini Observatory during the 2014B semester, and announced publicly in February 2015[57]. The impact of the defective amplifier is obvious in many spectra, and impacts $\sim$1/12 of any particular 2D spectrum. Unfortunately, this amplifier is located toward the middle of the detector array and covers wavelength ranges that include the 4000Å break and other important features for galaxies targeted in our program. The effect of the faulty amplifier on our final spectra varies significantly from mask to mask, and slit to slit. Wherever possible we exclude spectra from exposures where the amplifier effects are severe when stacking the individual 1D spectra for each slit, resulting in a modest loss in S/N for the affected spectra. As of late 2015 the faulty amplifier is repaired and will not be a problem for future observations.

4. PRIMARY SURVEY DATA PRODUCTS

4.1. Galaxy Redshift Measurements

We examine all calibrated, stacked, 1D spectra by eye, and estimate redshifts using one or more methods. Most redshift estimates use custom IDL code to cross-correlate strong, well-detected features typical of galaxy spectra such as the 4000Å break against the same features in template galaxy spectra; [O II] λ3727; Ca II H&Kλ3934, 3969; H-δ; H-γ; H-β; G-bandλ 4305; [O III] $\lambda\lambda$ 4960, 5007; and Mg I$\lambda\lambda\lambda$ 5169, 5174, 5185. In practice this means that we exclude regions of the spectral data that have low S/N, are contaminated by sky lines, or contain no notable spectral features. Independent redshift estimation was performed using the cross-correlation routines in the RVSAO IRAF package with the *fabtemp97* template (Kurtz & Mink 1998); the RVSAO routines are extremely similar, algorithmically, to our custom code, and results from the two methods are in excellent agreement, with typical uncertainties of $\delta cz \simeq 90 - 160$ km s^{-1}

---

[57] https://www.gemini.edu/pio/?q=node/10004

from both methods after correcting the RVSAO uncertainties up by a factor of 1.7 to accurately reflect the true cross-correlation uncertainties (Quintana et al. 2000).

In the case of galaxy spectra with low S/N or that only have one or more emission lines we fit Gaussian profiles to the available lines to estimate the galaxy redshift as the mean redshift of all individual lines, with the standard deviation between individual line measurements providing the galaxy redshift uncertainty. In cases where only one line is detected we use the uncertainty in the centroid of the Gaussian fit to that line to estimate the redshift uncertainty. Single-line redshifts are only measured for spectra with a clear emission line that can be confidently identified based on the lack of other strong emission features. For example, prominent nebular emission lines (i.e., [O II] $\lambda 3727$, H-β, [O III] 4960, 5007, and H-α) appear together in the spectra of star-forming galaxies, so that with the large wavelength coverage of our spectra we can often infer that a single emission line is [O II] $\lambda 3727$ — which is unresolved at our spectral resolution — with the redder nebular line redshifted out of our wavelength coverage.

Example cluster member spectra for SPT-GMOS resulting from standard MOS observations are shown in Figure 2, and N&S observations in Figure 3. In total we examine 3317 individual spectra, and measure high-confidence radial velocities for 2595 sources ($\sim$80% success rate). Of these sources we identify 352 as stars and 2243 as galaxies. These results only include high-confidence redshift measurements, as we generally do not report — or include in our data release — redshift interpretations that are significantly uncertain or unclear (i.e., "best-guess" redshifts). We do present a few of these best-guess redshifts in § 5.1, where we discuss the spectra of bright, strongly-lensed galaxies that were observed. We make this exception because exceptionally bright lensed sources are particularly rare objects, and any information or constraints on these sources can be useful for informing follow-up efforts.

4.1.1. *Redshifts of Giant Arcs*

Parallel to the primary objective of the SPT-GMOS survey program, we take every opportunity to place spectroscopic slits on other targets of high interest, such as candidate strongly-lensed sources in the cores of the target SPT clusters. Redshifts for these sources are estimated using one or both of: 1) our custom IDL cross-correlation code with either the Shapley et al. (2003) $z \sim 2 - 3$ composite spectrum or the Gemini Deep Deep Survey late-type $z \sim 1 - 2$ composite (GDDS; Abraham et al. 2004), and 2) fitting Gaussian profiles to families of typical strong ultraviolet (UV) absorption lines (e.g., Mg II 2796, 2803, Fe II 2344, 2372, 2384, 2586, 2600, C IV 1548, 1551, Si II 1260, 1527, and Si IV 1394, 1403) and measuring the mean and standard deviation in the individual line redshifts.

The spectra of some candidate strongly-lensed sources exhibit only weak continuum emission and do not have a clear redshift solution, but can have robust redshift constraints inferred from the combination of their blue colors and lack of emission lines (e.g., Bayliss et al. 2011a,b). For example, we expect a star-forming galaxy at $z \gtrsim 1.4$, observed over a range $\Delta\lambda \simeq 5000 - 9000$Å, to produce blue continuum emission with no strong emission
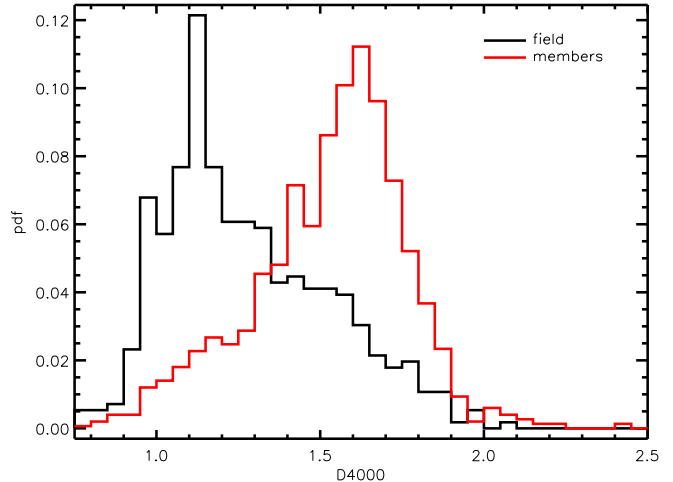
Fig. 6.— The distribution of values for the strength of the 4000Å break of both cluster member galaxies and non-cluster member galaxies.

lines; the most prominent features we would expect in such a spectrum would be absorption from low-ionization species in the inter-stellar medium, the strength of which can vary significantly from galaxy to galaxy and are often undetected in low S/N spectra. Similarly, in $\Delta\lambda \simeq 5000 - 9000$Å spectra of a star-forming galaxy at $z \gtrsim 3.1$ we would expect to see strong features associated with Lyman break galaxies (e.g., Shapley et al. 2003), the most prominent being strong absorption or emission from Ly-α. The absence of strong rest-frame optical emission lines and Ly-α in a given galaxy spectrum allows us to place lower and upper limits, respectively, on the redshift of that galaxy. The redshift interpretations of giant arcs observed in SPT-GMOS are described in more detail in § 5.1.

4.2. *Cluster Redshift and Velocity Dispersion Estimates*

The primary quantities that we want to measure for each galaxy cluster are the average cluster redshift, which reflects the bulk motion of the cluster in the Hubble Flow, and the velocity dispersion of cluster member galaxies, which scales with the depth of the cluster's gravitational potential. We follow the procedure described in Ruel et al. (2014), which includes first computing the average cluster redshift, $\bar{z}_{\mathrm{cluster}}$, using the bi-weight location estimator as formulated by Beers et al. (1990), and then compute the line-of-sight velocity dispersion for each cluster using two estimators: the square root of the bi-weight sample variance, $\sigma_{v,BI}$, and the gapper, $\sigma_{v,G}$ (Beers et al. 1990). Initial estimates of $\bar{z}_{\mathrm{cluster}}$, $\sigma_{v,BI}$ and $\sigma_{v,G}$ are generated by manually identifying each galaxy cluster as an over-density in velocity space and applying an initial rest-frame velocity cut of ± 5000 km s^{-1} relative to the starting guess of the cluster redshift. The choice of 5000 km s^{-1} is somewhat arbitrary, but our results are not sensitive to small changes in the choice of initial velocity cut. We then iteratively compute $\bar{z}_{cluster}$, $\sigma_{v,BI}$ and $\sigma_{v,G}$, applying rest-frame velocity cuts of $\pm 3\sigma_v$, where σ_v is set equal to $\sigma_{v,BI}$ when computed from ≥ 15 spectroscopic members, and equal to $\sigma_{v,G}$ when computed from < 15 members. The iterations continue

TABLE 3
SAMPLE SPT-GMOS DATA PRODUCTS FOR CANDIDATE BRIGHTEST CLUSTER GALAXY SPECTRA

Cluster Name	Object Name	RA (J2000.0)	Dec (J2000.0)	z (δ_z)[a]	W_0 [O II] $\lambda 3727$ (Å)	W_0 H-δ (Å)	D4000
SPT-CL J0013-4906	J001319.19-490638.8	00:13:19.19	-49:06:38.8	0.40998(15)	5.66 ± 1.50	-3.02 ± 1.32	1.64 ± 0.03
SPT-CL J0033-6326	J003353.01-632641.4	00:33:53.01	-63:26:41.4	0.59784(54)	1.48 ± 1.31	-1.57 ± 1.02	1.70 ± 0.02
SPT-CL J0102-4603	J010242.71-460416.0	01:02:42.71	-46:04:16.0	0.84008(64)	1.93 ± 2.61	-5.01 ± 2.08	1.68 ± 0.03
SPT-CL J0106-5943	J010628.73-594313.6	01:06:28.73	-59:43:13.6	0.35043(36)	1.06 ± 0.53	-2.40 ± 0.97	1.88 ± 0.01
SPT-CL J0118-5156	J011824.77-515628.7	01:18:24.77	-51:56:28.7	0.70210(99)	4.85 ± 3.07	-3.50 ± 2.54	1.53 ± 0.04
SPT-CL J0123-4821	J012310.92-482122.1	01:23:10.92	-48:21:22.1	0.65420(45)	1.71 ± 1.18	-2.03 ± 0.76	1.77 ± 0.02
SPT-CL J0142-5032	J014209.68-503231.6	01:42:09.68	-50:32:31.6	0.67872(82)	-3.26 ± 3.93	1.76 ± 2.14	1.79 ± 0.06
SPT-CL J0200-4852	J020034.09-485215.7	02:00:34.09	-48:52:15.7	0.49851(12)	5.20 ± 2.57	-2.86 ± 0.80	2.34 ± 0.23
SPT-CL J0205-6432	J020507.84-643226.9	02:05:07.84	-64:32:26.9	0.74300(25)	4.17 ± 1.69	0.24 ± 1.75	1.85 ± 0.03
SPT-CL J0212-4657	J021223.57-465713.9	02:12:23.57	-46:57:13.9	0.65725(06)	3.51 ± 59.08	-6.56 ± 1.52	1.73 ± 0.02
SPT-CL J0233-5819	J023300.97-581937.0	02:33:00.97	-58:19:37.0	0.66000(25)	1.98 ± 1.36	-1.74 ± 1.38	1.81 ± 0.03
SPT-CL J0243-4833	J024338.85-483339.1	02:43:38.85	-48:33:39.1	0.49693(34)	0.53 ± 1.25	-0.13 ± 0.56	1.71 ± 0.02
SPT-CL J0243-5930	J024327.08-593100.6	02:43:27.08	-59:31:00.6	0.63366(26)	1.70 ± 1.50	-0.42 ± 0.84	1.72 ± 0.02
SPT-CL J0245-5302	J024524.82-530145.4	02:45:24.82	-53:01:45.4	0.30280(25)	3.91 ± 0.90	-1.74 ± 1.04	1.85 ± 0.02
SPT-CL J0252-4824	J025249.98-482458.4	02:52:49.98	-48:24:58.4	0.42226(19)	5.89 ± 1.51	-2.42 ± 1.18	1.81 ± 0.04
SPT-CL J0304-4401	J030416.89-440131.5	03:04:16.89	-44:01:31.5	0.45491(25)	1.53 ± 1.70	-0.76 ± 0.87	2.68 ± 0.28
SPT-CL J0307-6225	J030716.77-622647.3	03:07:16.77	-62:26:47.3	0.57801(40)	-5.92 ± 2.63	-0.21 ± 1.21	1.64 ± 0.02
SPT-CL J0310-4647	J031032.50-464708.0	03:10:32.50	-46:47:08.0	0.70644(49)	1.97 ± 1.39	-3.20 ± 0.89	1.75 ± 0.02
SPT-CL J0324-6236	J032412.27-623555.8	03:24:12.27	-62:35:55.8	0.74515(94)	-1.79 ± 2.60	-1.26 ± 1.67	1.73 ± 0.03
SPT-CL J0334-4659	J033410.97-465945.9	03:34:10.97	-46:59:45.9	0.48693(51)	-84.12 ± 3.71	-4.16 ± 1.18	1.55 ± 0.02
SPT-CL J0348-4515	J034817.09-451500.3	03:48:17.09	-45:15:00.3	0.36272(67)	2.93 ± 0.74	-1.56 ± 0.67	1.92 ± 0.02
SPT-CL J0352-5647	J035257.55-564751.6	03:52:57.55	-56:47:51.6	0.64855(33)	1.72 ± 2.12	-1.81 ± 1.16	1.63 ± 0.03
SPT-CL J0356-5337	J035621.45-533752.0	03:56:21.45	-53:37:52.0	1.03303(27)	-1.00 ± 3.38	-2.36 ± 2.46	2.04 ± 0.06
SPT-CL J0403-5719	J040352.63-571946.5	04:03:52.63	-57:19:46.5	0.45856(33)	-0.47 ± 0.89	-0.42 ± 0.98	1.02 ± 0.01
SPT-CL J0406-4805	J040655.26-480457.4	04:06:55.26	-48:04:57.4	0.73449(83)	4.07 ± 3.31	-2.78 ± 1.98	1.65 ± 0.04
SPT-CL J0411-4819	J041110.98-481939.3	04:11:10.98	-48:19:39.3	0.41948(40)	1.61 ± 0.84	-0.55 ± 1.12	1.73 ± 0.02
SPT-CL J0417-4748	J041723.07-474848.0	04:17:23.07	-47:48:48.0	0.58041(55)	-115.46 ± 63.13	1.79 ± 0.93	1.70 ± 0.02
SPT-CL J0438-5419	J043817.63-541920.6	04:38:17.63	-54:19:20.6	0.42170(50)	3.04 ± 1.80	-1.09 ± 1.14	2.05 ± 0.04
SPT-CL J0456-5116	J045628.11-511635.0	04:56:28.11	-51:16:35.0	0.56270(37)	0.54 ± 1.34	-2.64 ± 1.21	1.59 ± 0.02
SPT-CL J0511-5154	J051142.95-515436.6	05:11:42.95	-51:54:36.6	0.64880(50)	2.34 ± 1.55	-0.67 ± 1.46	1.68 ± 0.03
SPT-CL J0539-5744	J053959.92-574435.3	05:39:59.92	-57:44:35.3	0.76873(90)	2.53 ± 3.31	-3.29 ± 3.45	1.65 ± 0.06
SPT-CL J0542-4100	J054250.05-410000.4	05:42:50.05	-41:00:00.4	0.64176(35)	-0.07 ± 1.54	0.25 ± 0.91	1.74 ± 0.02
SPT-CL J0555-6406	J055524.99-640620.8	05:55:24.99	-64:06:20.8	0.34496(60)	0.58 ± 0.64	-1.04 ± 0.49	1.97 ± 0.01
SPT-CL J0655-5234	J065551.98-523439.2	06:55:51.98	-52:34:39.2	0.46816(28)	-2.39 ± 2.13	-0.93 ± 0.81	1.55 ± 0.02
SPT-CL J0655-5234	J065552.75-523403.3	06:55:52.75	-52:34:03.3	0.47286(54)	1.43 ± 1.38	-0.23 ± 1.25	1.79 ± 0.03
SPT-CL J2017-6258	J201753.08-625938.7	20:17:53.08	-62:59:38.7	0.53624(26)	1.09 ± 3.13	2.49 ± 2.55	1.65 ± 0.04
SPT-CL J2020-6314	J202008.39-631449.7	20:20:08.39	-63:14:49.7	0.53761(33)	1.19 ± 1.33	-0.51 ± 1.23	1.61 ± 0.03
SPT-CL J2026-4513	J202628.26-451359.6	20:26:28.26	-45:13:59.6	0.68694(12)	-3.35 ± 3.43	-0.54 ± 1.81	1.64 ± 0.03
SPT-CL J2030-5638	J203045.25-563755.8	20:30:45.25	-56:37:55.8	0.39321(32)	0.68 ± 2.66	-2.56 ± 1.51	1.88 ± 0.04
SPT-CL J2035-5251	J203510.69-525122.1	20:35:10.69	-52:51:22.1	0.53465(53)	1.65 ± 1.15	-0.29 ± 0.62	1.66 ± 0.02
SPT-CL J2058-5608	J205822.28-560847.2	20:58:22.28	-56:08:47.2	0.60610(50)	-58.69 ± 8.40	-4.12 ± 3.38	1.21 ± 0.04
SPT-CL J2115-4659	J211512.78-465847.5	21:15:12.78	-46:58:47.5	0.29587(31)	4.57 ± 0.74	-1.81 ± 0.53	2.06 ± 0.02
SPT-CL J2118-5055	J211853.67-505555.2	21:18:53.67	-50:55:55.2	0.62380(25)	4.63 ± 2.04	-2.24 ± 1.94	1.86 ± 0.04
SPT-CL J2136-4704	J213627.85-470505.7	21:36:27.85	-47:05:05.7	0.41710(50)	0.70 ± 1.51	-0.39 ± 0.93	1.74 ± 0.02
SPT-CL J2140-5727	J214033.43-572711.4	21:40:33.43	-57:27:11.4	0.40778(14)	-9.73 ± 0.88	-1.35 ± 0.67	1.77 ± 0.01
SPT-CL J2146-4846	J214605.93-484653.3	21:46:05.93	-48:46:53.3	0.61770(25)	3.91 ± 3.04	0.48 ± 1.10	1.81 ± 0.03
SPT-CL J2146-5736	J214648.41-573653.7	21:46:48.41	-57:36:53.7	0.61060(09)	-0.95 ± 1.73	-1.15 ± 1.60	1.51 ± 0.03
SPT-CL J2155-6048	J215554.65-604723.7	21:55:54.65	-60:47:23.7	0.53480(50)	0.90 ± 1.17	0.41 ± 8.18	1.77 ± 0.02
SPT-CL J2155-6048	J215555.47-604902.8	21:55:55.47	-60:49:02.8	0.54190(25)	2.41 ± 1.04	-0.53 ± 1.30	2.00 ± 0.02
SPT-CL J2159-6244	J215958.67-624514.0	21:59:58.67	-62:45:14.0	0.39186(29)	2.47 ± 0.60	-1.99 ± 0.58	1.84 ± 0.01
SPT-CL J2159-6244	J220005.53-624456.3	22:00:05.53	-62:44:56.3	0.39108(24)	2.74 ± 0.64	-1.69 ± 0.65	1.89 ± 0.01
SPT-CL J2222-4834	J222250.73-483435.5	22:22:50.73	-48:34:35.5	0.65122(58)	-9.84 ± 2.34	1.21 ± 1.34	1.41 ± 0.02
SPT-CL J2232-5959	J223233.83-595953.1	22:32:33.83	-59:59:53.1	0.59564(70)	5.37 ± 2.07	0.26 ± 1.53	1.62 ± 0.02
SPT-CL J2233-5339	J223315.62-533909.2	22:33:15.62	-53:39:09.2	0.43847(39)	1.27 ± 0.84	-1.32 ± 0.62	1.90 ± 0.02
SPT-CL J2218-4519	J221859.22-451852.0	22:18:59.22	-45:18:52.0	0.63555(41)	2.42 ± 0.94	-1.07 ± 0.69	1.70 ± 0.02
SPT-CL J2258-4044	J225848.27-404430.7	22:58:48.27	-40:44:30.7	0.89652(31)	2.72 ± 4.63	-1.78 ± 2.02	1.54 ± 0.04
SPT-CL J2301-4023	J230151.89-402339.7	23:01:51.89	-40:23:39.7	0.84165(41)	-50.13 ± 22.03	4.93 ± 3.28	1.38 ± 0.02
SPT-CL J2306-6505	J230653.57-650517.5	23:06:53.57	-65:05:17.5	0.52850(35)	2.93 ± 0.64	-0.33 ± 0.66	1.79 ± 0.01
SPT-CL J2325-4111	J232512.01-411156.5	23:25:12.01	-41:11:56.5	0.35390(25)	2.33 ± 0.90	-0.23 ± 10.45	2.01 ± 0.02
SPT-CL J2325-4111	J232511.71-411213.8	23:25:11.71	-41:12:13.8	0.36240(75)	3.31 ± 1.36	-0.98 ± 4.07	1.91 ± 0.03
SPT-CL J2335-4544	J233508.51-454420.8	23:35:08.51	-45:44:20.8	0.54592(63)	0.57 ± 1.43	-2.31 ± 1.45	1.69 ± 0.03
SPT-CL J2344-4243	J234443.90-424312.1	23:44:43.90	-42:43:12.1	0.59810(99)	-97.05 ± 3.74	-3.73 ± 1.04	0.90 ± 0.01

NOTE. — Example of the primary SPT-GMOS data product catalog for each individual galaxy with a spectroscopic redshift measurement. The catalog includes, from left to right, the cluster name, galaxy name, galaxy coordinates, galaxy redshift, the equivalent width of [O II] $\lambda 3727$, the equivalent width of H-δ and the strength of the 4000Å break.

[a] The measured redshift with the uncertainty in the last two digits given in parentheses.

until converging onto a single solution. The final SPT-GMOS median cluster redshift estimates inform a calibration of photometric redshifts measured from cluster red sequences for the full SPT-SZ cluster sample over a broad redshift range (Figure 4).

Table 2 gives the final estimated values of $\bar{z}_{cluster}$, $\sigma_{v,BI}$ and $\sigma_{v,G}$ for the 62 SPT-GMOS clusters with data taken and reduced. We also show the velocity histograms with dispersion estimates over-plotted in Figure 5. Velocity dispersion confidence intervals are computed to be $\pm 0.92\sigma_v/\sqrt{N_{Members} - 1}$, which accurately captures the total measurement confidence intervals including both statistical uncertainties as well as the systematic uncertainties from the estimators and the effects of membership selection (Ruel et al. 2014). For clusters with < 15 members the gapper estimate of the velocity dispersion is generally considered more reliable, and for clusters with ≥ 15 members the bi-weight estimator is likely the better choice (Beers et al. 1990; Ruel et al. 2014), though we note that the $\sigma_{v,BI}$ and $\sigma_{v,G}$ estimates are in excellent agreement for all 62 clusters measured (Table 2). We identify a total of 1579 cluster member galaxies across 62 galaxy clusters, consistent with our $N \gtrsim 25$ members per cluster goal (Ruel et al. 2014).

4.2.1. Normality of Cluster Galaxy Velocity Distributions

The velocity dispersion estimators that we apply to our redshift data make an implicit assumption about the underlying cluster velocity distributions. Specifically, we assume that they are Gaussian, which is not always the case. The empirical uncertainty formula that we apply does account, at least in part, for the additional average uncertainty in the velocity dispersion estimate that results from ity of cluster velocity distributions (Ruel et al. 2014), but it is also useful to test each individual cluster velocity distribution for evidence of non-Gaussianity. There are a number of different statistical tests that can be applied here, but the value of these tests varies strongly with the number of individual galaxy measurements that are available for a given galaxy cluster. Einasto et al. (2012), for example, restrict their analysis of velocity substructure and non-Gaussianity in massive clusters to systems with at least 50 members; none of the SPT-GMOS galaxy clusters meet this member galaxy threshold. In a systematic study of this topic Hou et al. (2009) find that some tests are "profoundly unreliable" when < 30 galaxy velocities are available, which is the case for 2/3 of our sample. Hou et al. (2009) do find, however, that the Kolmogorov and Anderson-Darling (AD) tests are robust even when applied to very small samples (down to at least $N = 5$). It has been shown that the AD test is among the most statistically powerful tests for detecting departure from normality, whereas the Kolmogorov is among the least powerful (Hou et al. 2009). We therefore compute the AD test statistic, in which A^{2*} for the ordered data, x_i, is defined as,

$$A^{2*} = A^2 \left(1 + \frac{0.75}{n} + \frac{2.25}{n^2}\right), \qquad (1)$$

where A^2 is given by,

$$A^2 = -n - \frac{1}{n}\sum_{i=1}^{n}(2i-1)(\ln \Phi(x_i) + \ln(1 - \Phi(x_{n+1-i}))), \quad (2)$$

$x_i \leq x < x_{i+1}$, and $\Phi(x_i)$ is the cumulative distribution function of the hypothetical underlying distribution. The probability that a velocity distribution tested in this way is non-Gaussian, α_{AD}, is easily computed (see Equation 17 in Hou et al. (2009)). The results of the AD test for all SPT-GMOS galaxy clusters are reported in Table 2, along with the implied probability that each cluster's velocity distribution is non-Gaussian. Two (nine) of the 62 SPT-GMOS clusters have velocity distributions that are discrepant from Gaussian distributions at the 3-σ (2-σ) level.

4.3. Galaxy Spectral Indices: [O II] $\lambda 3727$, H-δ, and D4000Å

GMOS spectra taken with the B600 (R400) grating cover wavelength ranges of $\Delta\lambda \simeq 2800$ (4200) Å; this broad coverage ensures that we sample several well-established spectral indices for the large majority of the SPT-GMOS galaxies. We can, therefore, generate catalogs of galaxies with spectral index measurements of nearly all of the galaxies with GMOS spectra. Two important features that we focus on here are the [O II] $\lambda 3727$ forbidden line and H-δ. We measure rest-frame equivalent widths for each of these features in every galaxy where we have both a redshift measurement and where the spectra cover the appropriate rest-frame wavelengths. The equivalent width of a transition with λ is defined by the equation,

$$W_\lambda = \int (1 - F_\lambda/F_{\rm cont})d\lambda \qquad (3)$$

where all quantities have been converted into the rest-frame. We compute W_0 for [O II] $\lambda 3727$ and H-δ using the well-established intervals that define the flux density per pixel in the spectral line, F_λ, and the flux density per pixel in the continuum, F_{cont}, from Balogh et al. (1999). We also compute the strength of the 4000Å break (D4000) using wavelength intervals also defined by Balogh et al. (1999). The distribution of D4000 values for cluster members — as defined during our iterative velocity dispersion estimation described above in § 4.2 — and non-members is shown in Figure 6. Using these standard index definitions ensures uniform measurements, independent of both spectral resolution and the S/N of the spectra. Sample measurements of redshift and spectral indices are presented in Table 3; this table is an abridged version of the complete dataset where here we only show one or two candidate BCG(s) for each cluster. For SPT-SZ galaxy clusters that appear in McDonald et al. (2016) we use the same BCG candidates, and we perform the same visual selection of candidate BCGs for the rest of the SPT-GMOS sample. Not all clusters have a single clear BCG, so that in some cases we flag multiple bright galaxies as possible BCGs; we also note that a few of the clusters have BCGs that were not given a slit during the mask design step.

5. SECONDARY SURVEY PRODUCTS

In this section we describe several additional ancillary and derived data products beyond the primary measurements described above. This includes reporting redshift measurements and redshift constraints (for spectra where
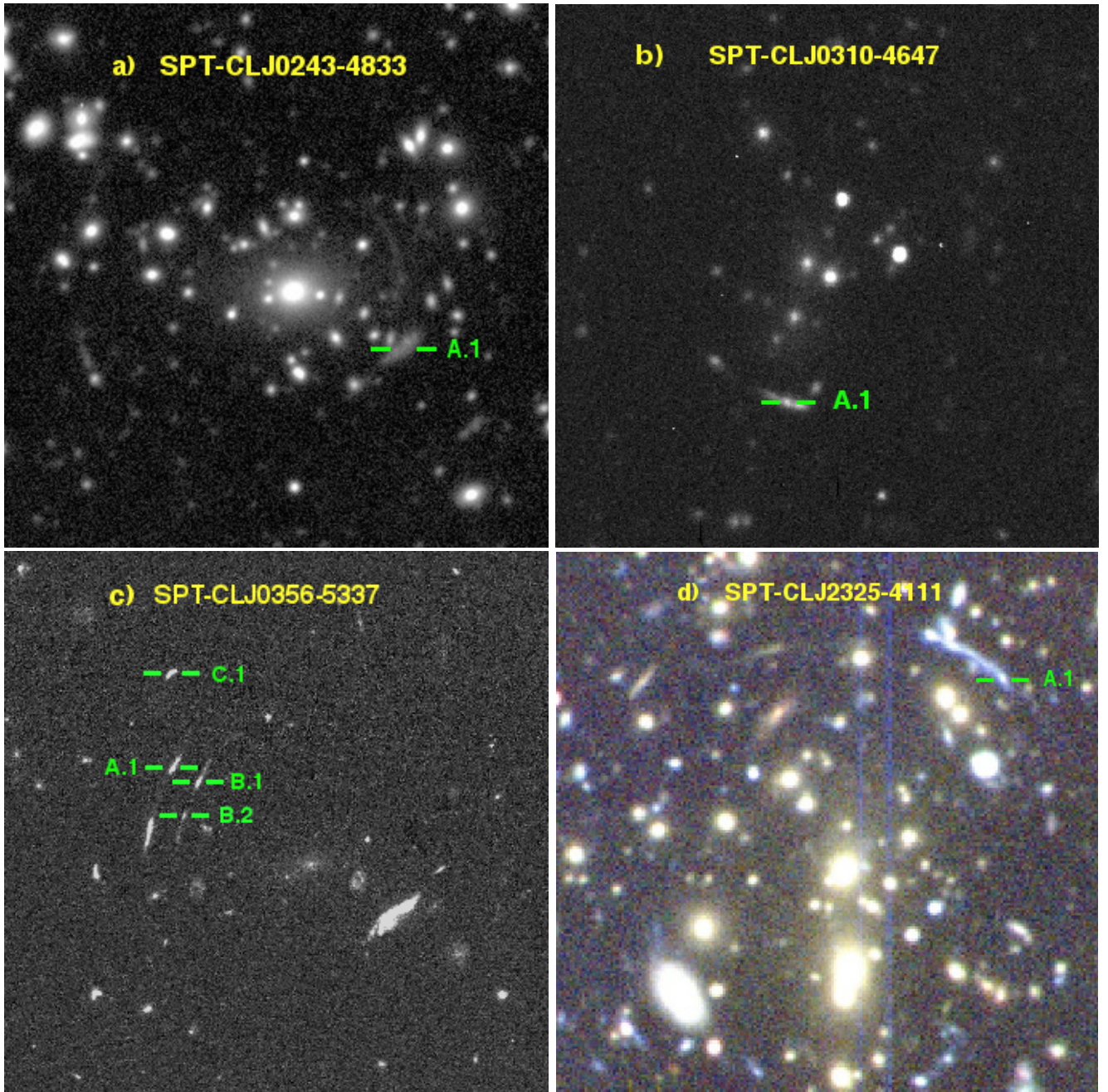
FIG. 7.— Optical images of SPT-GMOS clusters with candidate giant arcs for which we measure a robust redshift of at least one arc. We show the best-available imaging for showing the strong lensing features, which varies depending on the data available for each cluster. Horizontal green dashes indicate individual candidate strongly-lensed sources that were targeted by a slit in the SPT-GMOS program. Each targeted source is labeled, and the labels match those referred to in Table 4. North is up and East is to the left in each image. a) Magellan-II/MegaCam $r-$band image of the central $75'' \times 75''$ region of SPT-CL J0243-4833. b) Gemini/GMOS-South $r-$band image of the central $60'' \times 60''$ region of SPT-CL J0310-4647. c) HST/ACS F606W image of the central $40'' \times 40''$ region of SPT-CL J0356-5337. d) Magellan-II/PISCO (Stalder et al. 2014) gri-band image of the central $60'' \times 60''$ region of SPT-CL J2325-4111.

there is no clear redshift solution) for a sample of bright strongly lensed sources, matching the SPT-GMOS spectroscopic catalogs against photometric catalogs from previously published SPT-SZ follow-up, and derived properties of SPT-GMOS galaxies

5.1. Giant Arc Redshifts

We report new redshift measurements for several strongly-lensed background galaxies that appear near the cores of SPT galaxy clusters. New redshift constraints for giant arcs are given in Table 4, and images of each arc appear in Figures 7 & 8. The new SPT-GMOS giant arcs redshift measurements are consistent with the redshift distributions observed in other well-defined giant arc samples (Bayliss et al. 2011a; Bayliss 2012), and generally follow the peak era of unobscured star formation as traced by high surface brightness star-forming galaxies.

Bright strongly-lensed galaxies offer rare opportunities to study distant galaxies at a level of detail that is impossible in the field (Pettini et al. 2000; Bayliss et al.
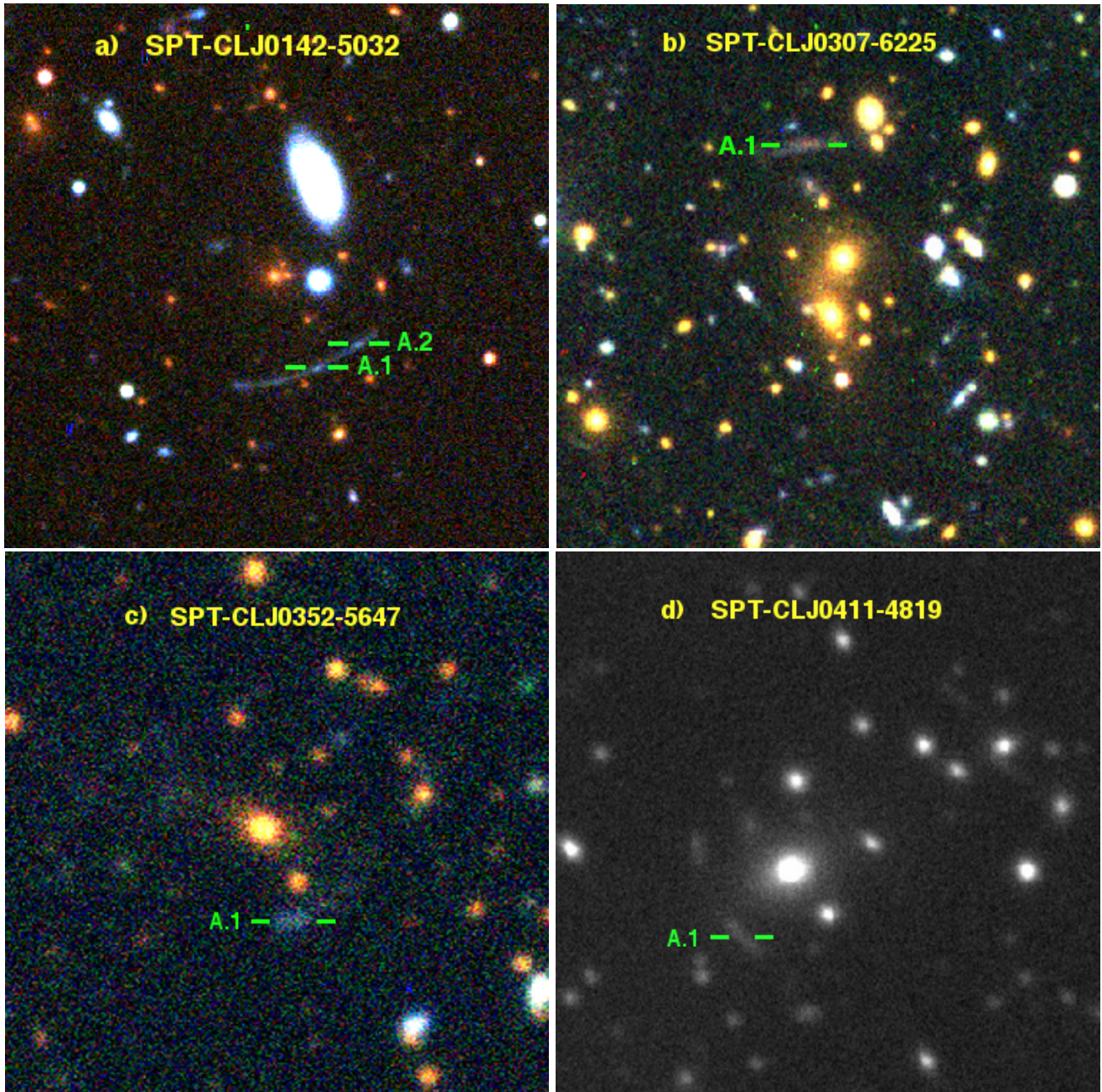
FIG. 8.— Optical images of SPT-GMOS clusters with candidate giant arcs where the spectra provide possible redshift measurements. Horizontal green dashes indicate individual candidate strongly-lensed sources that were targeted by a slit in the SPT-GMOS program. Each targeted source is labeled, and the labels match those referred to in Table 4. North is up and East is to the left in each image. a) Magellan-I/IMACS grz image of the central $75'' \times 75''$ region of SPT-CL J0142-5032. b) Magellan-II/LDSS3 gri image of the central $60'' \times 60''$ region of SPT-CL J0307-6225. c) Magellan-II/LDSS3 gri image of the central $60'' \times 60''$ region of SPT-CL J0352-5647. d) Gemini/GMOS-South $r-$band image of the central $60'' \times 60''$ region of SPT-CL J0411-4819.

2010; Bian et al. 2010; Koester et al. 2010; Wuyts et al. 2012; Bayliss et al. 2014b; James et al. 2014), and it is inevitable that the brightest high-redshift, strongly-lensed galaxies will be the most thoroughly studied and best-understood galaxies at their respective redshifts. Recent efforts have had great success finding the brightest strongly-lensed galaxies in wide-area surveys, primarily in the north. The new giant arcs presented here are a preliminary step toward extending the search for highly magnified distant galaxies into the south (e.g., Buckley-Geer et al. 2011; Nord et al. 2016), and will support

future strong lensing analyses of SPT strong lensing clusters, as well as tests of giant arc statistics within the SPT cluster sample.

5.1.1. *Giant Arc Redshift Measurements*

There are five giant arcs with SPT-GMOS spectra for which we report new spectroscopic redshift measurements. Three of these redshifts are unambiguous, but we consider the other two to be more speculative. The redshift interpretations of these five individual lensed galaxy spectra are briefly described below. We designate can-
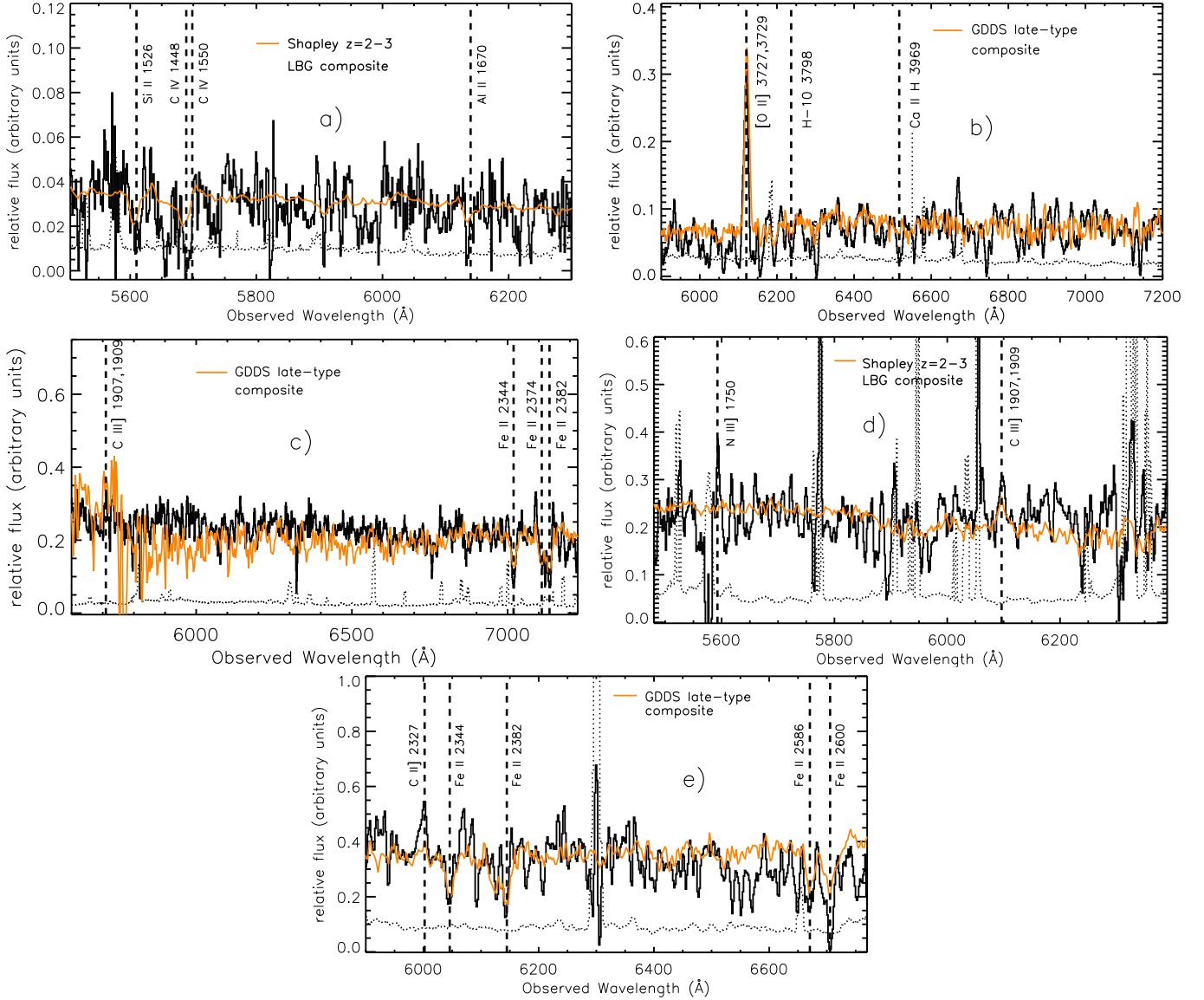
FIG. 9.— GMOS spectra (black solid line) of four giant arcs from which we measure redshifts, with the pixel-by-pixel uncertainties plotted as dotted lines. In each panel we also over-plot in orange one of either the Shapley et al. (2003) composite $z \simeq 2 - 3$ LBG composite spectrum, or the Abraham et al. (2004) GDDS $z \simeq 1 - 2$ late-type composite spectrum. a) Spectrum of A.1+A.2 in SPT-CL J0142-5032 with the Shapley et al. (2003) LBG composite redshifted to match that of the arc. b) Spectrum of A.1 in SPT-CL J0243-4833 with the GDDS late-type composite redshifted to match that of the arc. c) Spectrum of A.1 in SPT-CL J0356-5337 with the Shapley et al. (2003) LBG composite redshifted to match that of the arc. d) Spectrum of A.1 in SPT-CL J0310-4647 with the GDDS late-type composite redshifted to match that of the arc. e) Spectrum of A.1 in SPT-CL J2325-4111 with the GDDS late-type composite redshifted to match that of the arc.

didate strongly-lensed sources for each cluster, ordered arbitrarily, as A, B, C, etc., and indicate individual images as, for example, A.1 specifying the first image of the A lensed system, A.2 the second image, and so on (see Figure 7a-d, Figure 8a).

SPT-CL J0142-5032: This is a very low-confidence and speculative redshift solution owing to the low S/N ($\sim$ 1-1.5 per pixel) of the spectrum. The possible redshift solution is based on weak absorption features that coincide with strong lines common in Lyman break galaxies at $z = 2.674$. As shown in Figure 8a we targeted this arc with slits at two different positions and we see these very weak absorption features in the low S/N spectra from both slits. In Figure 9 we show a stack of the spectra from the two slit positions. Even if we are mis-

interpreting these weak features then we can still confidently conclude that this source falls within the redshift range, $1.44 < z < 3.1$, based on our wavelength coverage and the lack of strong spectral features.

SPT-CL J0243-4833: The strong [O II] $\lambda 3727$ emission line and accompanying weak absorption features (Ca II H $\lambda 3969$ and H-10 Balmer line) provide a robust redshift solution.

SPT-CL J0310-4647: We note strong C III] $\lambda 1909$ emission and a family of corroborating Fe II absorption lines; these features inform a clear redshift for the giant arc.

SPT-CL J0356-5337: The two possible emission lines identified here are very low-confidence, so we consider

TABLE 4
Giant Arc Redshift Constraints

SPT Cluster Lens	Arc ID	Slit RA (J2000.0)	Slit Dec (J2000.0)	Redshift	Spectral Features and Comments
Solid Redshifts:					
SPT-CL J0243-4833	A.1	02:43:37.36	-48:33:46.9	0.6418 ± 0.0003	[O II] $\lambda 3727$, H-10 $\lambda 3798$, Ca II $\lambda 3969$; Fig. 9
SPT-CL J0310-4647	A.1	03:10:32.27	-46:46:52.8	1.9942 ± 0.0002	C III] $\lambda\lambda 1907,1909$; Fe II $\lambda 2344$, 2374, 2382; Fig. 9
SPT-CL J2325-4111	A.1	23:25:10.20	-41:11:20.0	1.5790 ± 0.0010	C III] $\lambda\lambda 1907,1909$; Fe II $\lambda 2344$, 2382, 2586, 2600; Fig. 9
Possible Redshifts:				Best Guess z:	
SPT-CL J0142-5032	A.1	01:42:09.08	-50:32:42.0	2.6740 ± 0.0010	possible Si II $\lambda 1526$, C IV $\lambda 1550$, Al II $\lambda 1670$; Fig. 9
	A.2	01:42:08.52	-50:32:38.9	2.6740 ± 0.0010	possible Si II $\lambda 1526$, C IV $\lambda 1550$, Al II $\lambda 1670$; Fig. 9
SPT-CL J0356-5337	A.1	03:56:20.23	-53:37:53.6	2.1955 ± 0.0007	possible C III] $\lambda 1909$, N III] $\lambda 1750$; See Fig. 9
Redshift Limits:				z Constraints:	
SPT-CL J0142-5032	A.1	01:42:09.08	-50:32:42.0	$1.44 < z < 3.1$	$\Delta\lambda = 4900 - 9100$Å; see also best guess z above
	A.2	01:42:08.52	-50:32:38.9	$1.44 < z < 3.1$	$\Delta\lambda = 4900 - 9100$Å; see also best guess z above
SPT-CL J0307-6225	A.1	03:07:17.17	-62:26:28.9	$1.30 < z < 2.8$	$\Delta\lambda = 4430 - 8590$Å; weak continuum only
SPT-CL J0352-5647	A.1	03:52:57.13	-56:48:02.0	$1.40 < z < 3.0$	$\Delta\lambda = 4680 - 8980$Å; weak continuum only
SPT-CL J0356-5337	A.1	03:56:20.23	-53:37:53.6	$1.78 < z < 3.9$	$\Delta\lambda = 5920 - 10350$Å; see also best guess z above
	B.1	03:56:20.46	-53:37:55.2	$1.78 < z < 3.9$	$\Delta\lambda = 5920 - 10350$Å; weak continuum only
	B.2	03:56:20.46	-53:37:55.2	$1.78 < z < 3.9$	$\Delta\lambda = 5920 - 10350$Å; weak continuum only
	C.1	03:56:19.88	-53:37:58.9	$1.78 < z < 3.9$	$\Delta\lambda = 5920 - 10350$Å; weak continuum only
SPT-CL J0411-4819	A.1	04:11:10.59	-48:19:44.3	$0.84 < z < 2.3$	$\Delta\lambda = 3900 - 6850$Å; weak continuum only

Note. — Details of giant arcs observed in SPT-GMOS. Results are sorted into three categories. "Solid redshifts" are high-confidence measurements that appear in the SPT-GMOS spectroscopic catalogs. "Possible redshifts" are best-guess measurements and represent the most likely redshift for these sources based on a small number of very weak spectroscopic features, but could be mis-interpretations of the data. "Redshift limits" are constraints that we place on the redshifts of sources based on the *lack* of identifiable spectroscopic features in the available data.

this the most likely redshift for this source, but not an unambiguous redshift measurement. The possible N III] $\lambda 1750$ emission line, in particular, is at least as likely to be a noise spike as a real feature, because this line is not generally observed even in high S/N spectra of distant star-forming galaxies (e.g., Pettini et al. 2000; Shapley et al. 2003; Quider et al. 2009, 2010; Bayliss et al. 2014b). We only highlight this potential line in the figure because it does coincide quite well with the putative C III] $\lambda 1909$ emission feature. In the case where we are mis-interpreting these weak features we can still confidently conclude that this source falls within the redshift range, $1.78 < z < 3.9$, based on our wavelength coverage and the lack of strong spectral features.

SPT-CL J2325-4111: The spectrum exhibits strong C II] $\lambda 2326$ emission along with four strong Fe II absorption lines. These lines inform a clear redshift solution.

5.1.2. *Giant Arc Redshift Limits/Constraints*

There are also five giant arc candidates identified in four SPT-GMOS clusters that received spectroscopic slits but did not result in a precise redshift estimate. Instead we place redshift constraints on each of these sources based on the lack of strong spectral features in the GMOS spectra. Specifically, the arc candidates that we identify are blue, which would guarantee the presence of strong emission lines in their spectra, and if we detect continuum emission but fail to observe one or more of the rest-frame optical emission lines that are typical of blue star-forming galaxies in the spectrum of a given giant arc then we can conclude that it is at a sufficiently high redshift to move the bluest of those strong lines — [O II] $\lambda 3727$ — beyond the red end of our spectra. In the case of spectra that extend blueward of ~ 5000Å we can also place an upper limit on the redshift based on the lack of Ly-α observed either in emission or absorp-

tion (apparent as a strong spectral break). Giant arc candidates discussed below are shown in Figure 7c, and Figure 8b-d.

SPT-CL J0307-6225: We identify a blue, extended arc running tangentially relative to the center of the cluster. From the presence in its spectrum of low S/N continuum emission, the lack of emission lines, and the wavelength coverage ($\Delta\lambda = 4430 - 8590$Å) we infer that the arc has a redshift $1.30 < z < 2.8$.

SPT-CL J0352-5647: This cluster exhibits a blue extended source with a long but faint extended tail. In the spectrum of this source we again see weak continuum with no emission features, and from the wavelength coverage ($\Delta\lambda = 4680 - 8980$Å) we infer a redshift in the range $1.4 < z < 3$ for this source.

SPT-CL J0356-5337: We identify two strongly-lensed systems in this cluster — B and C, both having clear multiple images visible in *HST* imaging obtained as part of the SPT-SZ ACS Snapshot Survey (*HST* Program ID 13412, PI: Schrabback) — that received slit coverage on our spectroscopic masks but did not result in redshifts (Figure 9). The spectra of both the B and C sources exhibit low S/N blue continuum emission with no emission lines, and given the wavelength coverage ($\Delta\lambda = 5920 - 10350$Å) of the GMOS spectra we can infer that both sources have redshifts in the range, $1.78 < z < 3.9$.

SPT-CL J0411-4819: There is a clear giant arc candidate, consisting of at least two segments, near the core of this cluster. The spectrum of this source contains low S/N blue continuum emission with no emission lines, from which we infer a redshift in the range $0.84 < z < 2.3$ for the wavelength coverage ($\Delta\lambda = 5920 - 10350$Å) of the SPT-GMOS data.

TABLE 5
GALAXY SPECTRAL TYPE CLASSIFICATION

Spectral Type	$W_{0,3727}$ (Å)	$W_{0,H\delta}$ (Å)	Classification
k	none	< 3	passive
k+a	none	$\geq 3, \leq 8$	post-starburst
a+k	none	> 8	post-starburst
e(c)	> -40	< 4	star-forming
e(b)	≤ -40	any	star-forming
e(a)	yes	≥ 4	star-forming

NOTE. — This table lists the criteria used to classify galaxy type based on the strength of spectral features. The columns listed, from left to right, are the name of the specific galaxy spectral type, the criterion for the equivalent width of the [O II]λ 3727 feature, the criterion for the equivalent width of the H-δ feature, and the general classification (i.e., passive, post-starburst, or star-forming).

5.2. Magnitude Distribution of Cluster Members With Spectra

In addition to exploring their spectral types, it is also interesting to explore the distribution of galaxy magnitudes for which we measure spectra. Here we describe how the SPT-GMOS dataset can be combined with existing imaging catalogs of SPT-SZ galaxy clusters. This would enable, for example, systematic tests of velocity dispersion measurements such as investigating how velocity dispersion estimates change as a function of the fraction of brighter vs. fainter cluster member galaxies included. There is a large pool of optical imaging data available for the SPT-SZ galaxy cluster catalog (High et al. 2010; Song et al. 2012; Bleem et al. 2015), and we combine our spectra with these photometric measurements to determine the luminosities of those cluster member galaxies for which we now have spectra relative to the characteristic luminosity, $L^\star$ (or more precisely, its magnitude equivalent $M^\star$). The combination of broadband magnitudes and spectral line equivalent widths (§ 4.3) also provides a straightforward way to estimate spectral line fluxes, which can be used, for example, to estimate the instantaneous star formation rate from [O II] λ3727.

Most of the existing photometry is already in the Sloan Digital Sky Survey (SDSS; York et al. 2000) photometric system, but there is also a significant amount of imaging data that were taken using the older Johnson-Cousins filter sets ($BVRcIc$). Additionally, imaging acquired with the Swope 1m telescope Las Campanas is in a photometric system that is close to, but not precisely the same as Johnson-Cousins (Bleem et al. 2015). We use transformations determined empirically from standard star fields of the older photometric system that also appear in the SDSS (Jordi et al. 2006), which are optimized for stars rather than galaxies but are the only established transformations that use the photometric bands available to us. These transformations rely on applying an offset to a band that is closest to the SDSS band of interest, and then applying a color term. We are able to compute transformations into the SDSS $r-$band for all galaxies in our photometric catalogs, and are often but not always able to compute transformations into the SDSS $i-$band. Systematic uncertainties are unavoidable when applying these kinds of empirical transformations between photometric systems; Jordi et al. (2006) report systematic uncertainties of 0.06 magnitudes in their transformations between VRI and gri magnitudes, for instance. The
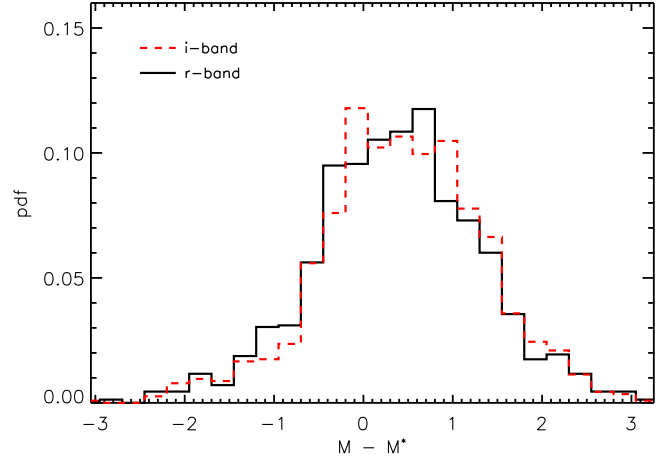
FIG. 10.— The distribution of magnitudes of cluster member galaxies with spectra measured in this work in the $r-$ and $i-$bands. Individual galaxies are plotted in units of magnitude minus the characteristic magnitude, M^*, at their redshift. The $r-$ and $i-$band magnitudes for individual galaxies are estimated using the procedure described in Section 5.2, such that data in various different optical bandpasses are all transformed into the SDSS $r-$ and $i-$bands.

transformed $r-$ and $i-$band magnitudes that we recover therefore have typical total uncertainties of $\sim$0.1 magnitudes.

The distribution of cluster member galaxy magnitudes, relative to m^* at each cluster redshift, is shown in Figure 10 for each of the $r-$ and $i-$bands. Recall that our mask design strategy focused on acquiring spectra for cluster members down to $\sim m^* + 1$, and that strategy is reflected in the magnitude distribution of spectroscopically-observed cluster galaxies, though we also find that we were able to measure redshifts for some cluster member galaxies as faint as $m^* + 2.5$. Having magnitudes in units of m^* in-hand for galaxies with spectroscopic data could be a valuable piece of information to fold into future analyses of galaxy cluster scaling relations involving velocity dispersions, as there is evidence from simulations that velocity dispersions can be biased by using only, for example, the very brightest cluster member galaxies (Saro et al. 2013; Gifford et al. 2013). This bias could potentially be removed from velocity dispersion estimates if we know the relative luminosities of the galaxies used to estimate the dispersion. We do point out, however, that while these magnitude-relative-to-m^* measurements inform us about the relative brightness of cluster member galaxies for which we have spectra, they *do not* fully characterize the *selection* function with respect to the luminosity of cluster galaxies with redshift measurements. Matched magnitudes for SPT-GMOS galaxies are available in the full SPT-GMOS data release (see § 2.1).

5.3. Galaxy Spectral Type Classification

Using the [O II] λ3727 doublet and the H-δ equivalent width data products described above it is straightforward to classify each galaxy with a GMOS spectrum and a spectroscopic redshift using the spectral index criteria described in Table 6 of Dressler et al. (1999). Table 5 lists the specific criteria that we use to classify SPT-GMOS galaxies as one of six types of galaxies; we apply these criteria exclusively to galaxy spectra that have reliable redshift measurements (2243 in total). Briefly,
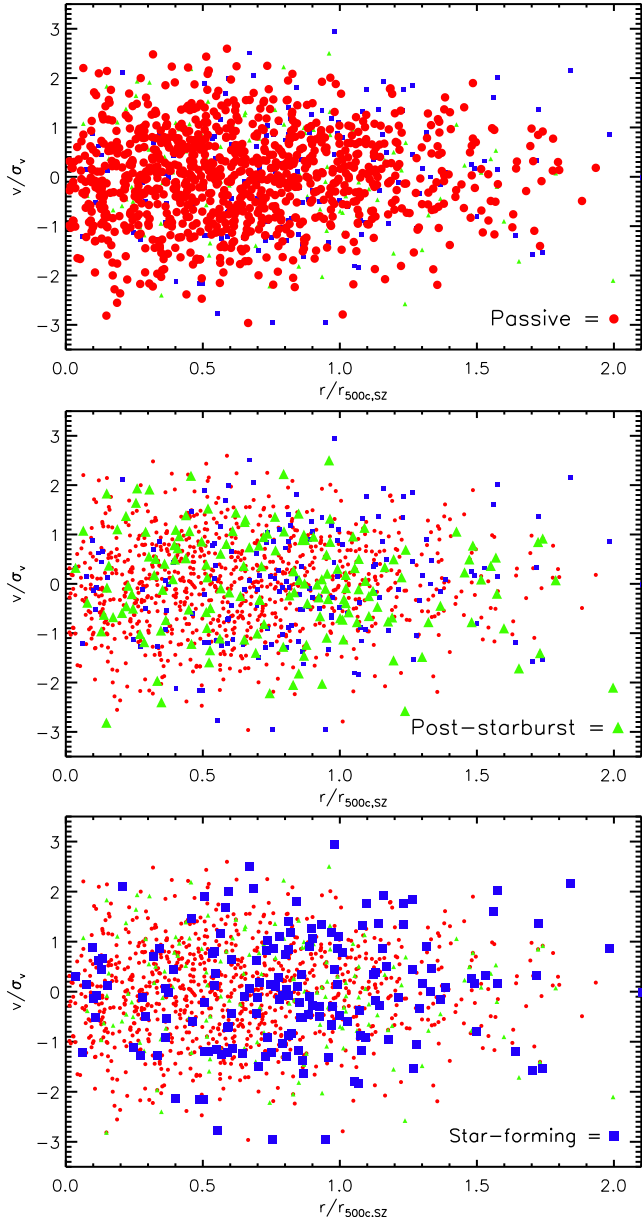
FIG. 11.— These three panels all show the full ensemble of member galaxies from all clusters within SPT-GMOS with each galaxy plotted according to its peculiar velocity relative to the median redshift of its host cluster. Individual galaxies are plotted in one of three colors indicating whether they were classified as passive (red), post-starburst (green), or actively star-forming (blue). In each panel we emphasize one galaxy type above the others: *Top:* passive galaxies, *Middle:* post-starburst galaxies, and *Bottom:* star-forming galaxies. The median projected radial distances of post-starburst and star-forming cluster members in the SPT-GMOS spectroscopic sample are both $\sim 0.9R_{500c,SZ}$, while for passive cluster members it is $\sim 0.67R_{500c,SZ}$.

these six spectral galaxy types identify a given galaxy as either passive (dominated by old stars), actively star-forming, or post-starburst (i.e., transitioning between star-forming and passive, with star formation likely recently quenched). Where the galaxy classification of [O II] $\lambda3727$ emission criteria reads "None", this refers to an absence of the [O II] $\lambda3727$ emission feature, or emission detected at $\leq 2\sigma$ significance, while "yes" refers to a detection of emission with $W_{0,3727} < 0$ at a significance of $> 2\sigma$. We identify no broad line emission objects — i.e.,

no strong active galactic nuclei (AGN) — in our spectra. Technically, because we target galaxies over a wide range of redshifts using masks that were observed with a wide range of different exposure times, our sensitivity to [O II] $\lambda3727$ emission varies somewhat across the SPT-GMOS sample, and no special effort was made to achieve a uniform effective detection limit in units of star formation (e.g., $M_\odot$ yr^{-1}). However, the SPT-GMOS program was designed to measure absorption line redshifts, and slits were deliberately placed on galaxies bright enough to produce decent S/N continuum spectra (S/N $\gtrsim 5$ per spectral element). This results in spectra that allow us to place useful limits on the presence of [O II] $\lambda3727$ emission in the vast majority of SPT-GMOS galaxy spectra. Exact depths vary from mask to mask due to variable observing conditions and differences between the photometric redshift used to plan the observations vs. the true redshifts of each galaxy cluster, but our spectra are typically sensitive down to $L_{[OII]} \simeq 5 - 10 \times 10^{40}$ erg s^{-1}, corresponding to a star formation rate, SFR$_{[OII]} \sim 1$ $M_\odot$ yr^{-1} (Kennicutt 1998).

Galaxy spectral type information is useful for exploring astrophysical trends such as the relationship between galaxy evolution with environment (e.g., Muzzin et al. 2013; Hennig et al. 2016; Zenteno et al. 2016). For example, Figure 6 demonstrates the difference in the distribution of D4000 values for SPT-GMOS galaxies in clusters vs. those in the field (i.e., non-cluster members as defined in § 4.2). The galaxy type information can also be used to investigate how cluster member galaxies of different spectral types occupy the phase space of line-of-sight velocity and projected radial distance from the galaxy cluster center. To demonstrate this we plot the ensemble of all SPT-GMOS galaxy cluster members, where each cluster member galaxy recession velocity is converted into a normalized peculiar velocity relative to the mean recession velocity/redshift of its host galaxy cluster, scaled into units of $\pm\sigma_v$. We also compute the projected physical radial distance between each cluster member and the SZ cluster centroids, normalized by $R_{500,SZ}$. With these quantities in-hand we can generate a sort of ensemble phase space for all SPT-GMOS galaxy clusters, which we show in Figure 11. Plotted in this way the SPT-GMOS sample of cluster members exhibits the same qualitative trends that have been observed in other studies (Mohr et al. 1996; Lewis et al. 2002; Rines et al. 2005; Pimbblet et al. 2006; Dressler et al. 2013), such as post-starburst and star-forming cluster member galaxies residing preferentially at larger cluster-centric radii. It is worth emphasizing the *qualitative* nature of this agreement, but we caution we note that the field of view of GMOS imposes an upper limit on the projected radial separation within which we have spectra for a given galaxy cluster. The precise limit varies with cluster mass and redshift, but generally prevented us from targeting galaxies with projected radial separations greater than $\sim 2R_{500,SZ}$. We note here the different *relative* median projected radii of different types of galaxies, but the specific median projected radii that we measure — $\sim 0.9R_{500c,SZ}$ for post-starburst and star-forming cluster members vs. $\sim 0.67R_{500c,SZ}$ for passive cluster members — do not necessarily represent the true median radial distributions of all cluster member galaxies.

These plots serve as an example of the kinds of analyses that the SPT-GMOS/ data products will enable, but we leave more rigorous analyses to future work, as the goal of this paper is to present the survey dataset and data products. The precise projected physical radii of SPT-GMOS galaxies are sensitive to the exact cosmological parameter values used to compute the angular diameter distance, and so we do not provide these values in the data release, but they are straightforward to compute from the galaxy positions (e.g., Table 3) and SPT-SZ galaxy cluster centroids provided in Table 1.

6. CONCLUSIONS AND SUMMARY

We present the full spectroscopic data release of the SPT-GMOS survey of 62 SPT-SZ galaxy clusters, which includes 2595 spectra with radial velocity measurements, 2243 of which are galaxies (1579 cluster members). Some of the SPT-SZ galaxy clusters are identified as strong-lensing systems in the available imaging, and we measure spectroscopic redshifts (or redshift constraints/limits) for candidate strongly-lensed background sources where possible. In addition to redshifts, we also measure standard spectral index measurements of the strength of the [O II] $\lambda 3727$ doublet, H-δ, and the 4000Å break. These indices are useful for spectrally classifying galaxies, and introduce the potential to investigate the properties of SPT-SZ member galaxies as a function of galaxy type.

The SPT-GMOS survey can be combined with previously published results from other spectroscopic programs (Sifón et al. 2013; Ruel et al. 2014; Sifón et al. 2016) to provide >100 SPT-SZ galaxy clusters with spectroscopic follow-up (longslit or MOS), and more than 90 clusters with $N \geq 15$ member velocity dispersion measurements. These data contribute to a broad effort to obtain multi-wavelength follow-up of SPT-SZ galaxy clusters — including extensive X-ray observations (Williamson et al. 2011; McDonald et al. 2013, 2014) and ongoing weak lensing measurements (e.g., High et al. 2012) — that will inform future multi-wavelength efforts to cross-calibrate the SZ mass-observable relation, and thereby enable future cosmological studies using galaxy clusters.

REFERENCES

Abell, G. O. 1958, ApJS, 3, 211
Abraham, R. G., et al. 2004, AJ, 127, 2455
Balogh, M., Babul, A., & Patton, D. 1999, MNRAS, 307, 463
Bayliss, M. B. 2012, ApJ, 744, 156
Bayliss, M. B., et al. 2014a, ApJ, 794, 12
Bayliss, M. B., Gladders, M. D., Oguri, M., Hennawi, J. F., Sharon, K., Koester, B. P., & Dahle, H. 2011a, ApJ, 727, L26+
Bayliss, M. B., Hennawi, J. F., Gladders, M. D., Koester, B. P., Sharon, K., Dahle, H., & Oguri, M. 2011b, ApJS, 193, 8
Bayliss, M. B., Rigby, J. R., Sharon, K., Wuyts, E., Florian, M., Gladders, M. D., Johnson, T., & Oguri, M. 2014b, ApJ, 790, 144
Bayliss, M. B., Wuyts, E., Sharon, K., Gladders, M. D., Hennawi, J. F., Koester, B. P., & Dahle, H. 2010, ApJ, 720, 1559
Beers, T. C., Flynn, K., & Gebhardt, K. 1990, AJ, 100, 32
Benson, B. A., et al. 2013, ApJ, 763, 147
Bian, F., et al. 2010, ApJ, 725, 1877
Bleem, L. E., et al. 2015, ApJS, 216, 27
Bocquet, S., et al. 2015, ApJ, 799, 214
Böhringer, H., et al. 2001, A&A, 369, 826
——. 2000, ApJS, 129, 435

Brodwin, M., et al. 2010, ApJ, 721, 90
Buckley-Geer, E. J., et al. 2011, ApJ, 742, 48
Burenin, R. A., Vikhlinin, A., Hornstrup, A., Ebeling, H., Quintana, H., & Mescheryakov, A. 2007, ApJS, 172, 561
Carlstrom, J. E., et al. 2011, PASP, 123, 568
Carlstrom, J. E., Holder, G. P., & Reese, E. D. 2002, ARA&A, 40, 643
Chant, C. A. 1930, JRASC, 24, 390
Chiu, I., et al. 2016, MNRAS, 455, 258
Colless, M., et al. 2001, MNRAS, 328, 1039
——. 2003, ArXiv Astrophysics e-prints
de Haan, T., et al. 2016, submitted
Dressler, A., Oemler, Jr., A., Poggianti, B. M., Gladders, M. D., Abramson, L., & Vulcani, B. 2013, ApJ, 770, 62
Dressler, A., Smail, I., Poggianti, B. M., Butcher, H., Couch, W. J., Ellis, R. S., & Oemler, Jr., A. 1999, ApJS, 122, 51
Drinkwater, M. J., et al. 2010, MNRAS, 401, 1429
Ebeling, H., Edge, A. C., Bohringer, H., Allen, S. W., Crawford, C. S., Fabian, A. C., Voges, W., & Huchra, J. P. 1998, MNRAS, 301, 881

Edge, A. C., Stewart, G. C., Fabian, A. C., & Arnaud, K. A. 1990, MNRAS, 245, 559
Einasto, M., et al. 2012, A&A, 540, A123
Eisenhardt, P. R. M., et al. 2008, ApJ, 684, 905
Eisenstein, D. J., et al. 2011, AJ, 142, 72
——. 2005, ApJ, 633, 560
Foley, R. J., et al. 2011, ApJ, 731, 86
Geller, M. J., Dell'Antonio, I. P., Kurtz, M. J., Ramella, M., Fabricant, D. G., Caldwell, N., Tyson, J. A., & Wittman, D. 2005, ApJ, 635, L125
Geller, M. J., Diaferio, A., Rines, K. J., & Serra, A. L. 2013, ApJ, 764, 58
Geller, M. J., & Huchra, J. P. 1989, Science, 246, 897
Geller, M. J., Hwang, H. S., Fabricant, D. G., Kurtz, M. J., Dell'Antonio, I. P., & Zahid, H. J. 2014, ApJS, 213, 35
Gifford, D., Miller, C., & Kern, N. 2013, ApJ, 773, 116
Gladders, M. D., & Yee, H. K. C. 2000, AJ, 120, 2148
Hamuy, M., Suntzeff, N. B., Heathcote, S. R., Walker, A. R., Gigoux, P., & Phillips, M. M. 1994, PASP, 106, 566
Hamuy, M., Walker, A. R., Suntzeff, N. B., Gigoux, P., Heathcote, S. R., & Phillips, M. M. 1992, PASP, 104, 533
Hasselfield, M., et al. 2013, JCAP, 7, 8
Hennig, C., et al. 2016, ArXiv e-prints, 1604.00988
High, F. W., et al. 2012, ApJ, 758, 68
——. 2010, ApJ, 723, 1736
Hook, I. M., Jørgensen, I., Allington-Smith, J. R., Davies, R. L., Metcalfe, N., Murowinski, R. G., & Crampton, D. 2004, PASP, 116, 425
Hou, A., Parker, L. C., Harris, W. E., & Wilman, D. J. 2009, ApJ, 702, 1199
Hubble, E., & Humason, M. L. 1931, ApJ, 74, 43
Jackson, J. C. 1972, MNRAS, 156, 1P
James, B. L., et al. 2014, MNRAS, 440, 1794
Jordi, K., Grebel, E. K., & Ammon, K. 2006, A&A, 460, 339
Kaiser, N. 1987, MNRAS, 227, 1
Kennicutt, Jr., R. C. 1998, ARA&A, 36, 189
Kirk, B., et al. 2015, MNRAS, 449, 4010
Koester, B. P., Gladders, M. D., Hennawi, J. F., Sharon, K., Wuyts, E., Rigby, J. R., Bayliss, M. B., & Dahle, H. 2010, ApJ, 723, L73
Koester, B. P., et al. 2007, ApJ, 660, 239
Kurtz, M. J., & Mink, D. J. 1998, PASP, 110, 934
Lewis, A. D., Ellingson, E., & Stocke, J. T. 2002, ApJ, 566, 771
Majumdar, S., & Mohr, J. J. 2003, ApJ, 585, 603
——. 2004, ApJ, 613, 41
Marriage, T. A., et al. 2011, ApJ, 737, 61
McDonald, M., et al. 2014, ApJ, 794, 67
——. 2013, ApJ, 774, 23
——. 2016, ApJ, 817, 86
Mohr, J. J., Geller, M. J., Fabricant, D. G., Wegner, G., Thorstensen, J., & Richstone, D. O. 1996, ApJ, 470, 724
Muzzin, A., Wilson, G., Demarco, R., Lidman, C., Nantais, J., Hoekstra, H., Yee, H. K. C., & Rettura, A. 2013, ApJ, 767, 39
Nord, B., et al. 2016, ApJ, 827, 51
Oke, J. B. 1990, AJ, 99, 1621
Pacaud, F., et al. 2016, A&A, 592, A2

Percival, W. J., & White, M. 2009, MNRAS, 393, 297
Pettini, M., Steidel, C. C., Adelberger, K. L., Dickinson, M., & Giavalisco, M. 2000, ApJ, 528, 96
Pimbblet, K. A., Smail, I., Edge, A. C., O'Hely, E., Couch, W. J., & Zabludoff, A. I. 2006, MNRAS, 366, 645
Planck Collaboration, et al. 2014, A&A, 571, A20
Quider, A. M., Pettini, M., Shapley, A. E., & Steidel, C. C. 2009, MNRAS, 398, 1263
Quider, A. M., Shapley, A. E., Pettini, M., Steidel, C. C., & Stark, D. P. 2010, MNRAS, 402, 1467
Quintana, H., Carrasco, E. R., & Reisenegger, A. 2000, AJ, 120, 511
Reichardt, C. L., et al. 2013, ApJ, 763, 127
Rines, K., Geller, M. J., Diaferio, A., & Kurtz, M. J. 2013, ApJ, 767, 15
Rines, K., Geller, M. J., Kurtz, M. J., & Diaferio, A. 2003, AJ, 126, 2152
——. 2005, AJ, 130, 1482
Rosati, P., Della Ceca, R., Norman, C., & Giacconi, R. 1998, ApJ, 492, L21
Rozo, E., et al. 2010, ApJ, 708, 645
Ruel, J., et al. 2014, ApJ, 792, 45
Rykoff, E. S., et al. 2014, ApJ, 785, 104
Sadeh, I., Feng, L. L., & Lahav, O. 2015, Physical Review Letters, 114, 071103
Saro, A., Mohr, J. J., Bazin, G., & Dolag, K. 2013, ApJ, 772, 47
Schaffer, K. K., et al. 2011, ApJ, 743, 90
Shapley, A. E., Steidel, C. C., Pettini, M., & Adelberger, K. L. 2003, ApJ, 588, 65
Sifón, C., et al. 2016, MNRAS, 461, 248
——. 2013, ApJ, 772, 25
Song, J., et al. 2012, ApJ, 761, 22
Stalder, B., et al. 2013, ApJ, 763, 93
Stalder, B., Stark, A. A., Amato, S. M., Geary, J., Shectman, S. A., Stubbs, C. W., & Szentgyorgyi, A. 2014, in Proc. SPIE, Vol. 9147, Ground-based and Airborne Instrumentation for Astronomy V, 91473Y
Staniszewski, Z., et al. 2009, ApJ, 701, 32
Sunyaev, R., & Zel'dovich, Y. 1980, ARAA, 18, 537
Sunyaev, R. A., & Zel'dovich, Y. B. 1972, Comments on Astrophysics and Space Physics, 4, 173
van Dokkum, P. G. 2001, PASP, 113, 1420
Vanderlinde, K., et al. 2010, ApJ, 722, 1180
von der Linden, A., et al. 2014, MNRAS, 443, 1973
Wen, Z. L., Han, J. L., & Liu, F. S. 2012, ApJS, 199, 34
White, M., Cohn, J. D., & Smit, R. 2010, MNRAS, 408, 1818
Williamson, R., et al. 2011, ApJ, 738, 139
Wojtak, R., Hansen, S. H., & Hjorth, J. 2011, Nature, 477, 567
Wuyts, E., Rigby, J. R., Gladders, M. D., Gilbank, D. G., Sharon, K., Gralla, M. B., & Bayliss, M. B. 2012, ApJ, 745, 86
York, D. G., et al. 2000, AJ, 120, 1579
Zenteno, A., et al. 2016, ArXiv e-prints, 1603.05981
——. 2011, ApJ, 734, 3